ARTICLES
PUBLISHED ONLINE: 18 APRIL 2016 | DOI: 10.1038/NMAT4624
nature materials

Bioresorbable silicon electronics for transient spatiotemporal mapping of electrical activity from the cerebral cortex

Ki Jun Yu[1,2†], Duygu Kuzum[3,4,5†], Suk-Won Hwang[6], Bong Hoon Kim[2,7], Halvor Juul[8], Nam Heon Kim[2,7], Sang Min Won[1,2], Ken Chiang[9], Michael Trumpis[9], Andrew G. Richardson[4,10], Huanyu Cheng[11], Hui Fang[2,7], Marissa Thompson[3,4,12], Hank Bink[3,4], Delia Talos[8], Kyung Jin Seo[2,7], Hee Nam Lee[2,13], Seung-Kyun Kang[2,7], Jae-Hwan Kim[2,7], Jung Yup Lee[2,13], Younggang Huang[14], Frances E. Jensen[4,8], Marc A. Dichter[4,8], Timothy H. Lucas[4,10], Jonathan Viventi[9], Brian Litt[3,4,8*] and John A. Rogers[1,2,7*]

Bioresorbable silicon electronics technology offers unprecedented opportunities to deploy advanced implantable monitoring systems that eliminate risks, cost and discomfort associated with surgical extraction. Applications include postoperative monitoring and transient physiologic recording after percutaneous or minimally invasive placement of vascular, cardiac, orthopaedic, neural or other devices. We present an embodiment of these materials in both passive and actively addressed arrays of bioresorbable silicon electrodes with multiplexing capabilities, which record *in vivo* electrophysiological signals from the cortical surface and the subgaleal space. The devices detect normal physiologic and epileptiform activity, both in acute and chronic recordings. Comparative studies show sensor performance comparable to standard clinical systems and reduced tissue reactivity relative to conventional clinical electrocorticography (ECoG) electrodes. This technology offers general applicability in neural interfaces, with additional potential utility in treatment of disorders where transient monitoring and modulation of physiologic function, implant integrity and tissue recovery or regeneration are required.

Neurophysiologic monitoring is commonly used for diagnosing and treating neurological disorders such as epilepsy, Parkinson's disease, depression, chronic pain and disorders of the peripheral nervous system[1,2]. Such capabilities are critically important for mapping and monitoring brain function during and in preparation for resective neurosurgery[3], such as for epilepsy and tumours, for assisting in neurodevice placement, such as for Parkinson's disease[4], epilepsy[5] and depression, and for guiding surgical procedures on complex, interconnected peripheral nerve structures, such as the brachial, lumbar and sacral plexi[2]. Related functionality is also increasingly leveraged during intravascular procedures, such as aneurysm coiling[6], stent placement[7], arteriovenous malformation (AVM) embolization[8], and endoscopic operations. Post-procedure monitoring typically occurs in an intensive care unit (ICU), where a variety of devices record physiological activity, typically with limited temporal and spatial sampling, directly at the regions of interest, simply because these are exposed and accessible during surgery[9]. Intracranial monitors for postoperative seizures and recovery of brain function after surgery would also be useful, and potentially more sensitive than scalp monitoring[10]. These clinical needs motivate efforts to develop technologies for neurophysiologic monitoring that incorporate inorganic and organic nanomaterials in flexible formats[11–20]. Although it would be desirable for neuromonitoring in the ICU to offer the same high-fidelity, high-resolution performance as is available in the operating room, the morbidity and cost associated with additional surgeries to remove implanted recording devices preclude this possibility in general practice. In certain cases, such as in invasive intracranial electrocorticographic monitoring for epilepsy surgery, recording electrodes remain in place for one to three weeks to localize epileptic networks[21]. Here, removal occurs in a second procedure, often with resection of brain involved in generating seizures. In other cases, electrodes are placed in staging procedures that do not end in resection, but rather are done for

[1]Department of Electrical and Computer Engineering, University of Illinois at Urbana-Champaign, Urbana, Illinois 61801, USA. [2]Frederick Seitz Materials Research Laboratory, University of Illinois at Urbana-Champaign, Urbana, Illinois 61801, USA. [3]Department of Bioengineering, University of Pennsylvania, Philadelphia, Pennsylvania 19104, USA. [4]Center for Neuroengineering and Therapeutics, University of Pennsylvania, Philadelphia, Pennsylvania 19104, USA. [5]Department of Electrical and Computer Engineering, University of California, San Diego, San Diego, California 92093, USA. [6]KU-KIST Graduate School of Converging Science and Technology, Korea University, Seoul 136-701, Republic of Korea. [7]Department of Materials Science and Engineering, University of Illinois at Urbana-Champaign, Urbana, Illinois 61801, USA. [8]Department of Neurology, Perelman School of Medicine, University of Pennsylvania, Philadelphia, Pennsylvania 19104, USA. [9]Department of Biomedical Engineering, Duke University, Durham, North Carolina 27708, USA. [10]Department of Neurosurgery, Perelman School of Medicine, University of Pennsylvania, Philadelphia, Pennsylvania 19104, USA. [11]Department of Engineering Science and Mechanics, Penn State University, University Park, Pennsylvania 16802, USA. [12]Department of Chemical and Biomolecular Engineering, University of Pennsylvania, Philadelphia, Pennsylvania 19104, USA. [13]Department of Chemical and Biomolecular Engineering, University of Illinois at Urbana-Champaign, Urbana, Illinois 61801, USA. [14]Department of Mechanical Engineering and Department of Civil and Environmental Engineering, Northwestern University, Evanston, Illinois 60208, USA. [†]These authors are contributed equally to this work. *e-mail: littb@upenn.edu; jrogers@illinois.edu

© 2016 Macmillan Publishers Limited. All rights reserved

broad lateralization in preparation for more extensive implants or placement of implantable devices. Here, a second procedure to remove implants adds cost and risk. Recent evidence suggests that one to three months of ambulatory intracranial recording may be required to adequately localize seizures for epilepsy surgery or device placement, a period prohibitively long for existing in-hospital approaches[22]. Using bioresorbable electrodes for such studies would eliminate the danger and cost of removing electrodes at the end of this period, during which standard devices may become fibrosed or adherent to underlying tissues. An ideal scenario would involve placement of temporary, bioresorbable monitoring systems capable of providing continuous streams of data for guiding medical care over predetermined periods of time before dissolving. Below we present a new class of technology that offers this mode of operation, with spatiotemporal resolution that matches or exceeds any existing alternative.

Recently reported bioresorbable sensors of pressure and temperature in the intracranial space provide distinct, complementary capabilities in single-point measurements of non-electrical characteristics of the cerebrospinal fluid in the intracranial space[23]. Here, we introduce materials and device designs for direct electrical interfaces to the brain itself, including bioresorbable electrodes and multiplexing electronics for high-speed spatiotemporal mapping of biological processes. The platform builds on recently described technologies that exploit nanomembranes of device-grade, monocrystalline silicon (Si NMs) as the semiconductor foundation of a high-performance class of flexible electronic systems. The key enabling chemistry involves hydrolysis of Si NMs following immersion in biofluids, to yield end products that are biocompatible. The results presented here indicate that Si NMs, at high levels of doping[24], can also serve as the neural recording electrodes themselves, as a stable, yet ultimately transient, measurement interface. In addition to their established bioresorbability, the nanoscale thicknesses of Si NMs, when deployed with thin substrates, interconnect metals and dielectrics, yield devices with levels of mechanical flexibility necessary for conformal contact and chronically stable interfaces with neural tissues. The following content describes means to exploit these concepts in materials, devices and system-level examples of bioresorbable Si electronic interfaces to the brain, in passive and active matrix-addressed recording *in vivo*. Evaluations include capture of ECoG and subdermal encephalograms (EEG) in live, awake animal models, where Si NMs serve as active materials both for the recording interface and for the backplane transistors that allow high-speed multiplexed addressing across arrays of channels. Comprehensive *in vitro* and *in vivo* studies establish that these systems provide accurate and reproducible measurements of neural signals and physiological activity for acute (~h) and chronic (up to 33 days) use. Biocompatibility studies reveal no overt tissue reactions compared to clinically approved commercial ECoG electrodes.

Figure 1a provides an exploded schematic diagram (left) and a magnified optical microscope image of the active sensing and the passivation regions (right) of a simplest embodiment of these concepts: a thin, flexible electrode array based on a phosphorus-doped (impurity concentrations: $\sim 10^{20}$ cm^{-3}) collection of Si NMs (thickness ~300 nm) structures. Here, a layer of SiO_2 (thickness ~100 nm) insulates the connection traces to isolate them from biofluids and adjacent tissue. The terminal pads consist of exposed Si, as the direct neural interface. A flexible sheet of the bioresorbable polymer poly(lactic-co-glycolic acid, PLGA, thickness ~30 μm) serves as the substrate. This array (3×4 mm^2) allows chronic recordings from rat cortex at four measurement sites, each with dimensions of 250×250 μm^2. Such small arrays serve effectively in demonstrator experiments and studies of the fundamental issues in the materials science. We note, however, that the materials and fabrication schemes align with those used in the semiconductor industry and are, as a result, immediately scalable to much larger areas, higher channel counts and smaller/larger electrode sizes. As an illustration, Fig. 1b (bottom panels) presents a passive array that includes 256 independent channels, in a 16×16 configuration, with an overall area of 3 cm × 3.5 cm. Multiplexing architectures, described subsequently, provide routes to scaling to even higher numbers of channels. The fabrication steps appear in the Methods and in Supplementary Fig. 1. The lot and functional electrode yields are ~100% and >90%, respectively. Figures 1b (top) and Supplementary Fig. 2 show micrographs of completed arrays. Figure 1b (bottom) shows a scaled version of this same basic device architecture that includes 256 independent channels.

Placing an array onto a hydrogel substrate (Fig. 1c) and immersing the system in phosphate-buffered saline (PBS) at physiological pH (7.4) and at room temperature enables characterization of each of the electrodes by electrochemical impedance spectroscopy (EIS), across a range of frequencies most relevant to the studies described subsequently. In the recording of brain signals, the electrodes transduce ionic currents in the electrolyte to an electric current in the measurement system. The contact between an electrode and tissue has an associated electrical impedance, where reductions in the impedance decrease the noise level, thereby increasing the signal-to-noise ratio (SNR) of the recordings[19,25]. The data in Fig. 1d correspond to the impedance ($|Z|$) of each channel in the array, along with the response of a gold (Au) electrode with the same dimensions. The EIS data for Si can be fitted to an equivalent Randles circuit model (Supplementary Fig. 3a) that includes a double-layer capacitance (C_{PE}) in parallel with a charge transfer resistance (R_{CT}), all of which is in series with a resistance (R_S) that corresponds to the surrounding electrolyte solution. This model quantitatively captures the EIS data for both Au (without the space charge layer) and Si electrodes, as shown in Supplementary Fig. 3b. The fitted values of C_{PE} are ~2.5 μF cm^{-2} and ~10 μF cm^{-2} for Si and Au, respectively; both values are in a range consistent with the literature[26,27]. The space charge layer lowers the capacitance of the Si electrode[28], causing the differences between the Au and Si electrodes (Fig. 1d). More details of *in vitro* experiments of the Si electrodes are described in Supplementary Note 1 and Supplementary Figs 4–7.

The slow, controlled dissolution of Si NMs is critically important in their use as bioresorbable neural interfaces. Bioresorbable metals are less attractive options owing to their comparatively fast dissolution kinetics, and tendency to crack, fragment and flake during the process. Si dissolves under physiological conditions by hydrolysis to yield silicic acid, at rates that depend strongly on the ionic content of the surrounding solution, pH, temperature and other factors, including the doping level. Specifically, Si forms neutral ortho-silicic acid $Si(OH)_4$ through an initial oxidation step to SiO_2 or through a direct equilibrium $Si + 4H_2O \leftrightarrow Si(OH)_4 + 2H_2$ (refs 29,30). Figure 1e illustrates the dissolution kinetics for highly boron-doped and phosphorus-doped (concentration of $\sim 10^{20}$ cm^{-3}) Si NMs (~300 nm thick) in artificial cerebrospinal fluid (aCSF, pH 7.4) at physiological temperature (37 °C), evaluated by measuring the thicknesses at different time points by profilometry (Dektak, USA). Observations indicate that dissolution occurs in an exceptionally controlled, predictable process, without the cracks, flakes, particulates or reduction in surface smoothness that often occur in dissolution of metals. The dissolution rate exhibits a constant, thickness-independent value of ~11 nm d^{-1} for these conditions. The dissolution characteristics of the other materials in the system, which for the case of the simple device in Fig. 1 are SiO_2 and PLGA, are also important, although less critical than the Si NMs owing to their passive role in the device operation. Measurements indicate that SiO_2 and PLGA (75:25; ref. 31) dissolve in biofluids at 37 °C at rates of ~8.2 nm d^{-1}

© 2016 Macmillan Publishers Limited. All rights reserved

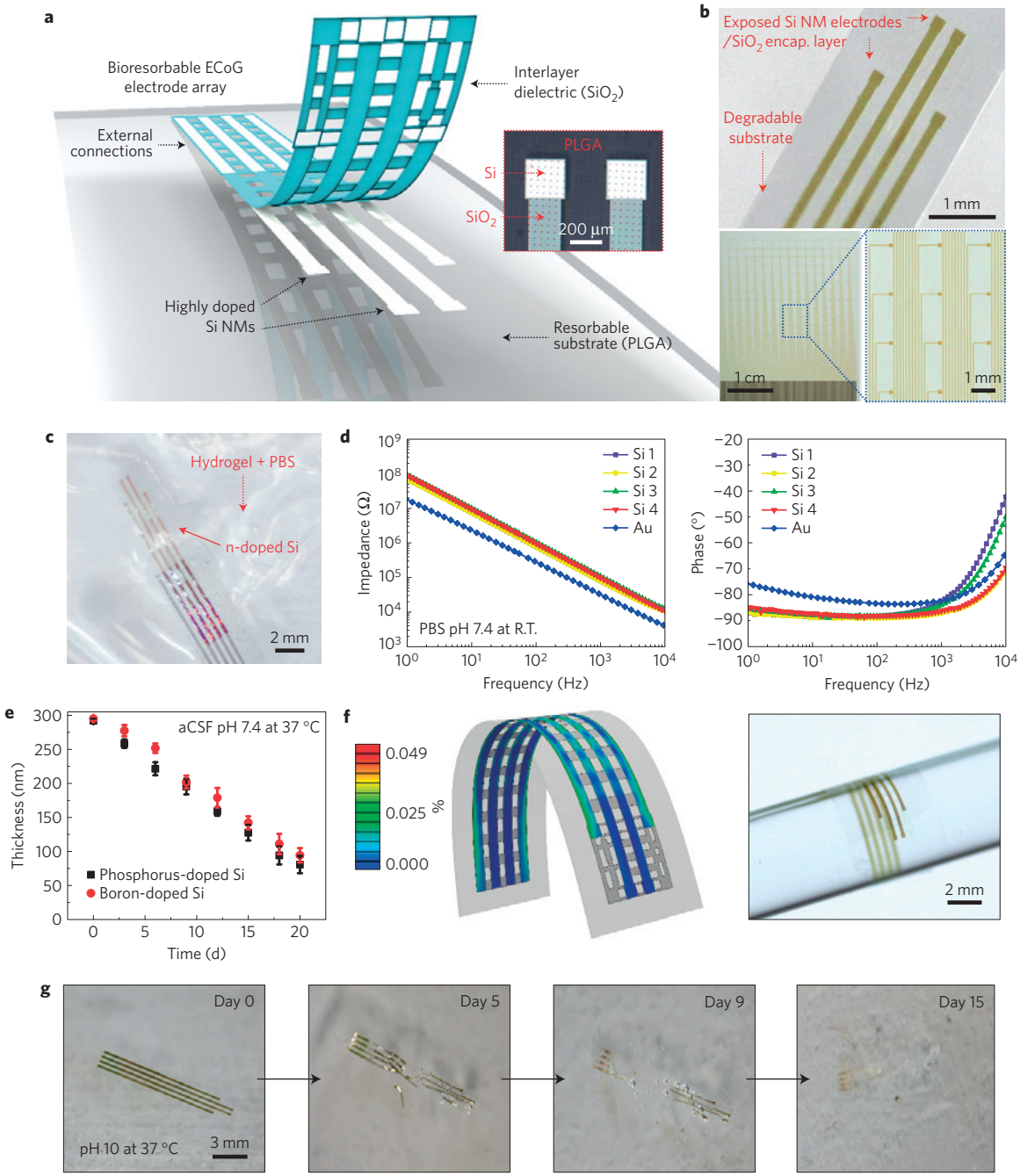

Figure 1 | Thin, flexible neural electrode arrays with fully bioresorbable construction based on patterned silicon nanomembranes (Si NMs) as the conducting component. a, Schematic exploded-view illustration of the construction of a passive, bioresorbable neural electrode array for ECoG and subdermal EEG measurements. A photolithographically patterned, n-doped Si NM (~300 nm thick) defines the electrodes and interconnects. A film of SiO_2 (~100 nm thick) and a foil of PLGA (~30 μm thick) serve as a bioresorbable encapsulating layer and substrate, respectively. The device connects to an external data acquisition (DAQ) system through an anisotropic conductive film interfaced to the Si NM interconnects at contact pads at the edge. A magnified optical image of electrodes on the right highlights the sensing (Si NMs) and insulating (SiO_2) regions. **b**, Photographs of bioresorbable neural electrode arrays with 4 channels (top) and 256 (16 × 16 configuration) channels (bottom). **c**, Microscope image of a device on a hydrogel substrate immersed in an aqueous buffer solution (pH 7.4) at 37 °C. **d**, Electrochemical impedance spectra, magnitude (left) and phase (right), measured at four different recording sites in an array configured for ECoG. **e**, Dissolution kinetics for phosphorus-doped and boron-doped Si NMs (~300 nm thick, dopant concentration 10^{20} cm^{-3}) during immersion in artificial cerebrospinal fluid (aCSF) pH 7.4 at 37 °C. **f**, Distribution of principal strains extracted from finite-element modelling (FEM) of a device bent to a radius of curvature of 1 mm (centre) and corresponding displacement profile (left) and image of an array wrapped around a cylindrical tube with a radius of 2 mm (right). **g**, Images collected at several stages of accelerated dissolution induced by immersion in an aqueous buffer solution (pH 10) at 37 °C.

(Supplementary Fig. 8), and complete dissolution timescales of ~4–5 weeks, respectively. Results of accelerated dissolution tests appear in Fig. 1g as a series of images of a complete device collected at various times after immersion in PBS pH 10 at 37 °C. We estimate that the present device designs and material choices allow complete dissolution of the device in two months. Si and SiO_2 will dissolve

© 2016 Macmillan Publishers Limited. All rights reserved

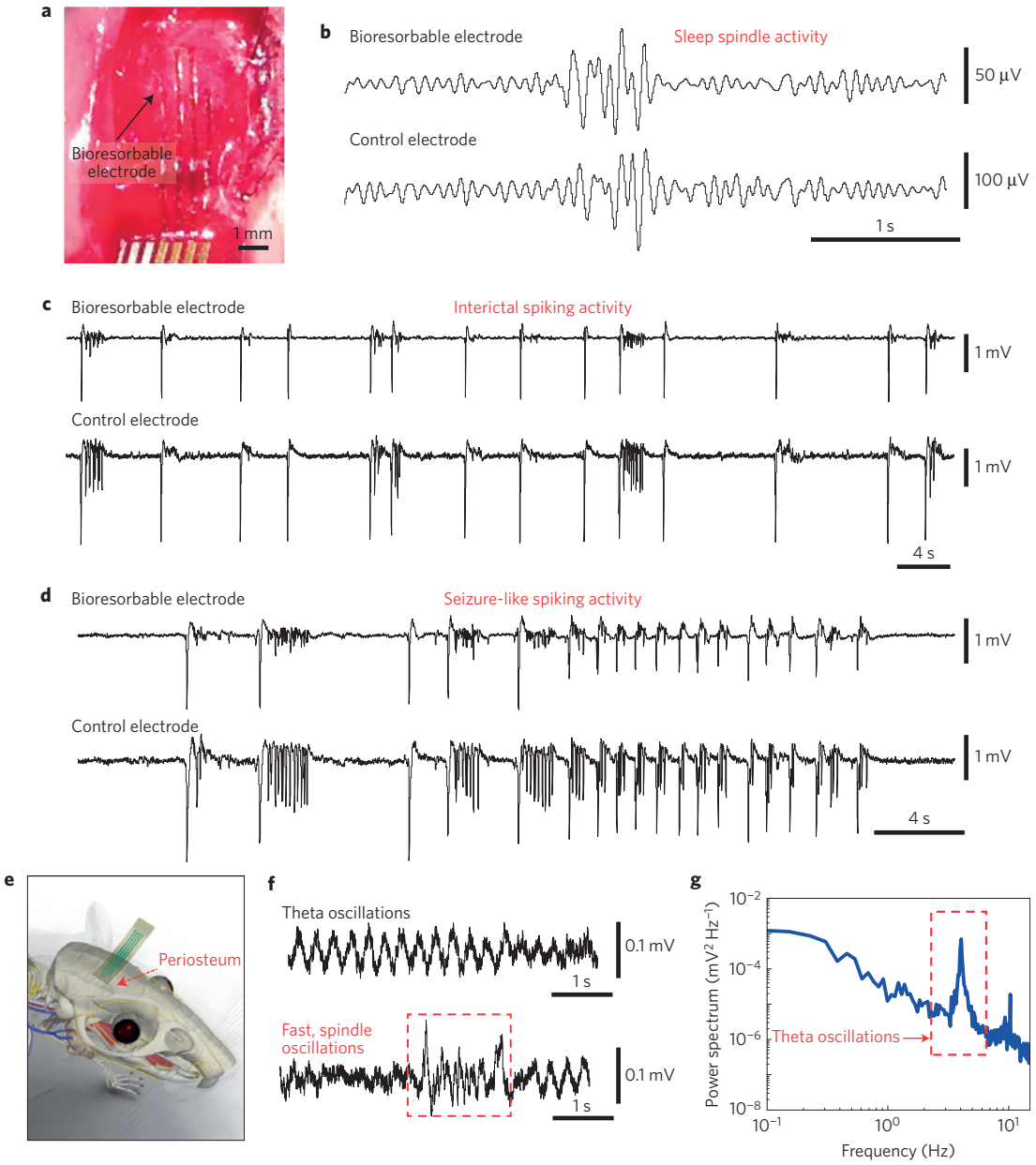

Figure 2 | *In vivo* neural recordings in rats using a passive, bioresorbable electrode array. The data presented here are representative of three separate acute experiments, each with a duration of ~5–6 h. **a**, Photograph of a four-channel bioresorbable electrode array placed on the cortical surface of the left hemisphere of a rat. **b**, Sleep spindles recoded by a bioresorbable electrode and a nearby commercial stainless steel microwire electrode, as a control placed at a depth of 0.5 mm from the cortical surface. **c**, Interictal spiking activity captured by the bioresorbable electrode and the control electrode after topical application of bicuculline methodide. Both electrodes interface with the same hemisphere. Data were processed through a 0.1 Hz–5 kHz bandpass filter. Recordings by the bioresorbable electrode and the control electrode show consistent interictal spikes. **d**, Interictal spiking activity recorded by the bioresorbable electrode and the control electrode 30 min after topical application of bicuculline methodide. Both recordings exhibit a high signal-to-noise ratio (Si: 42, control electrodes: 32) for detecting epileptiform activity. **e**, Cartoon illustration of a bioresorbable array placed on the periosteum for subdermal EEG recordings. **f**, Theta oscillations and fast spindle-like oscillations recorded subdermally using bioresorbable electrodes during isoflurane anaesthesia. **g**, Power density spectra of the theta oscillations recorded over a 5 min time window. The spectrum shows a clear peak at the expected frequency range.

within a month and two weeks, respectively, followed by PLGA. PLGA will dissolve in ~4–5 weeks. The materials parameters (that is, thicknesses, doping levels for the Si, and ratio of lactide to glycolide for the PLGA) can be adjusted to achieve desired dissolution times.

For conformal contact against the curved surface of the brain, thin geometries and optimized mechanical layouts are important. Three-dimensional finite-element modelling (FEM) reveals distributions of principal strain for bending perpendicular to the interconnect direction, as in Fig. 1f (left). On the basis of the layouts and the mechanical moduli, the maximum strains in the SiO_2, Si and PLGA are less than 0.03% for a bending radius of 1 mm, corresponding to the linear elastic regime for each of these materials. An optical image of a device wrapped around a glass rod with a radius of curvature of ~2 mm appears in Fig. 1f (right). Measurements before and after bending show negligible differences

© 2016 Macmillan Publishers Limited. All rights reserved

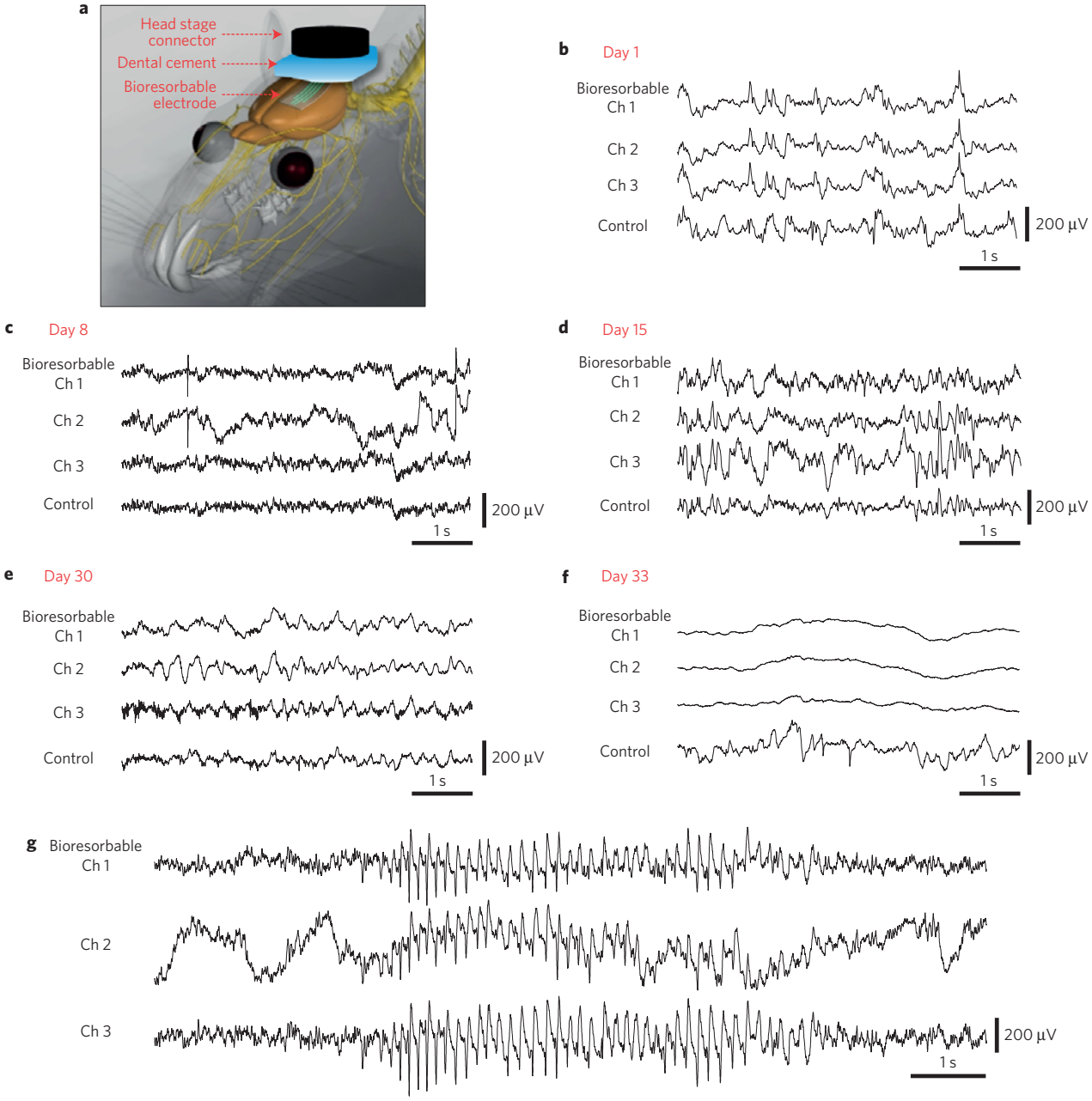

Figure 3 | *In vivo* chronic recordings in rats using a passive, bioresorbable electrode array. The data presented here are representative of chronic recording experiments with a duration of 30 days. **a**, Cartoon illustration of a four-channel bioresorbable electrode array implanted on the left hemisphere of the brain of a rat, for chronic recordings. A flexible ACF cable connects the array to a custom-built circular interface board fixed to the skull using dental cement. **b**–**f**, Representative ECoG signals recorded by the bioresorbable array and the control electrode on days 1, 8, 15, 30 and 33. Recordings from three electrodes from the bioresorbable array exhibit large-scale oscillatory behaviour consistent with small local and temporal variations. After functional dissolution (day 33), signals from the bioresorbable array show no ECoG activity, whereas the control electrode continues to show expected cortical potentials. **g**, High-voltage rhythmic spikes observed during absence-like seizure activity recorded chronically.

in impedance, consistent with expectations based both on FEM and analytical modelling results (Supplementary Fig. 9).

In vivo neural recording experiments involved the bioresorbable devices of Fig. 1 in adult rat animal models anaesthetized and placed in a stereotaxic apparatus. A craniotomy exposed a $4 \times 8\,mm^2$ region of cortex in the left hemisphere (Fig. 2a), to allow positioning of a device on an area of the cortical surface next to a standard stainless steel microelectrode ($7{,}850\,\mu m^2$) as a control for recording physiological oscillations under isoflurane anaesthesia. Figure 2b shows representative sleep spindle activity captured by one of the channels in the bioresorbable array and the control electrode. Supplementary Fig. 10 shows similar data for brain waves recorded during transition to deep anaesthesia (Supplementary Fig. 10a) and K-complexes (Supplementary Fig. 10b) measured under anaesthesia. Representative examples of pre-ictal and ictal-like spiking epileptiform activity induced by application of crystals of bicuculline methoxide recorded by the bioresorbable electrode and the control electrode appear in Fig. 2c,d, respectively. The frequency of the pre-ictal spikes (Fig. 2c) increases and the inter-spike duration decreases as the time progresses, terminating into after-discharges

© 2016 Macmillan Publishers Limited. All rights reserved

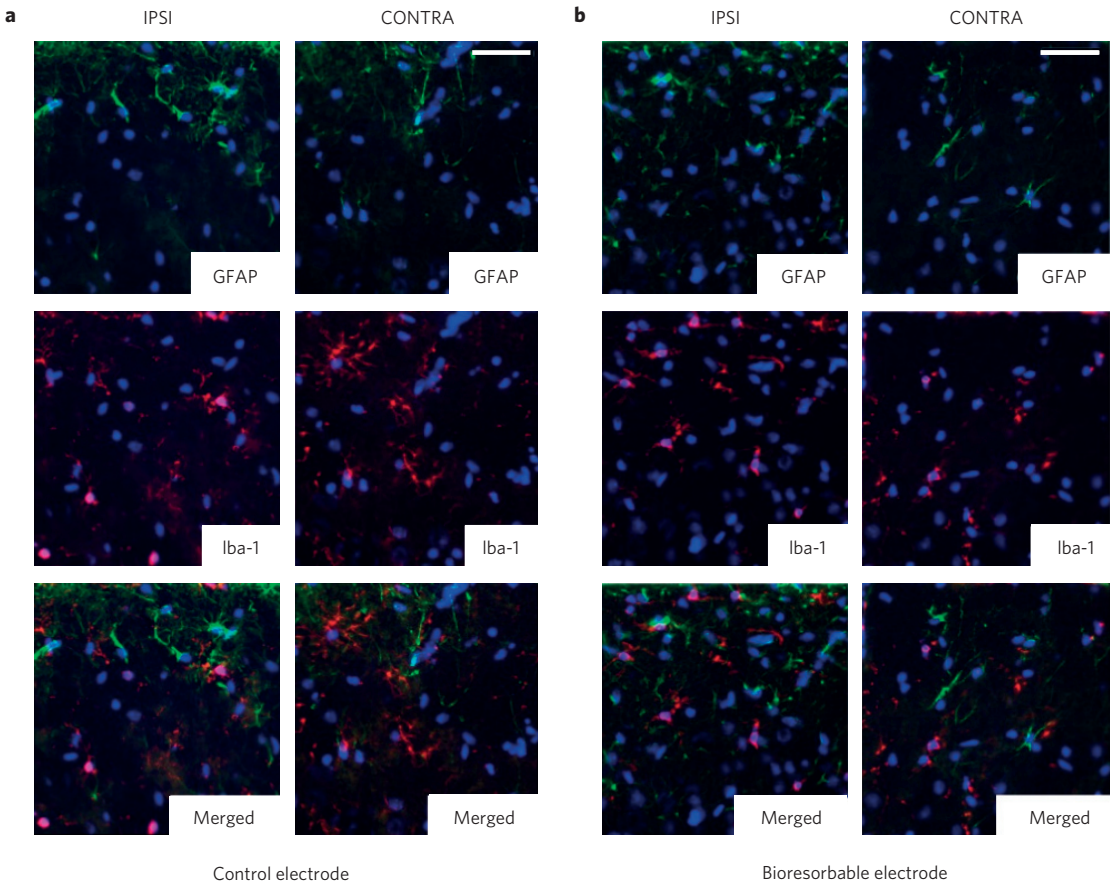

Figure 4 | Immunohistology analysis. a,**b**, Double-labelling for astrocytic marker GFAP (green) and microglia/macrophages marker Iba-1 (red) demonstrates moderate subpial gliosis at the implantation sites of both control (**a**, top) and bioresorbable (**b**, top) electrodes, and a marked increase in the densities of activated round microglial cells, exclusively underneath the control electrodes (**a**, middle). Cell nuclei are visualized with DAPI stain (blue). Scale bars represent 30 μm.

and ictal-like early epileptic discharges (Fig. 2d). The bioresorbable arrays can also be used as subdermal implants for high-fidelity recording of EEG and evoked potentials. Devices implanted on the periosteum, as described in Fig. 2e and Supplementary Fig. 11, yielded reliable recordings of theta waves (highlighted in power spectral analysis) and sleep spindles (Fig. 2f). Collectively, the results demonstrate that bioresorbable recording platforms can capture reliable physiological or pathological activity both intracortically and subdermally.

Chronic tests of ECoG recording indicate long-term stability in operation, where devices with increased thicknesses of SiO_2 (~300 nm) and Si NMs (~1,000 nm) survive for more than one month. Such studies used a miniature interface board connected to the device via a flexible interconnect cable to a headstage (Supplementary Fig. 12) designed for use with rats. Details are explained in the Methods. Figure 3 summarizes representative cortical potentials recorded by three electrodes in the bioresorbable array and by a nearby screw electrode as a control, captured on Days 1, 8, 15, 30, 32 (Supplementary Fig. 13), and 33 measured from the time of the surgical implantation. Figure 3a and Supplementary Figs 12 and 14 describe the surgical procedures and the post-surgical set-ups used in freely moving rats, respectively. ECoG potentials show physiological signals and brain oscillations with various temporal and spatial differences. High-amplitude seizure-like rhythmic spike discharges (Fig. 3g) appear occasionally, consistent with absence-like seizure activity observed in Long Evans Rats[32–34]. By all functional metrics (for example, signal-to-noise ratio, ability to measure delta, theta, alpha, gamma, spindles and sometimes epileptic spikes), the devices operate in a stable fashion, largely without change in performance throughout the month of the study, until sudden failure, probably due to the development of an open circuit state in the vicinity of the interconnects. After day 33, signals from the bioresorbable device disappear; whereas those from the control persist, consistent with dissolution of at least some critical component of the device. For epilepsy patients, the clinically relevant operational lifetime is several weeks. Here, bioresorbable monitors could be embedded into particular clinical devices to monitor for early signs of failure during critical postoperative periods, such as measuring pressure and flow after intravascular aneurysm occlusion (coiling), placement of aortic or other vascular grafts, or procedures to seal cerebrospinal fluid (CSF) leaks. At present, monitoring is based on clinical examination, or requires interventional radiology that is invasive, expensive and impractical for continuous monitoring over days to months.

Understanding the reactive tissue response is critical in assessing the potential for use in such clinical applications[35]. Tissue inflammation, encapsulation of the electrodes in fibrous tissue (glial scar) and neuronal death in the vicinity of the electrode are the most important issues related to clinical translation[36–38]. Studies of tissue reactions of bioresorbable electrode arrays involved chronic implants in 14 animals, with Pt electrodes cut into similar geometries from clinical subdural grids (Ad-Tech Medical) as controls, as shown in Supplementary Fig. 15. Figure 4 summarizes the results obtained according to procedures outlined in the Methods. Double-label immunohistochemistry for GFAP and Iba-1 reveal glial cell activation at four weeks

© 2016 Macmillan Publishers Limited. All rights reserved

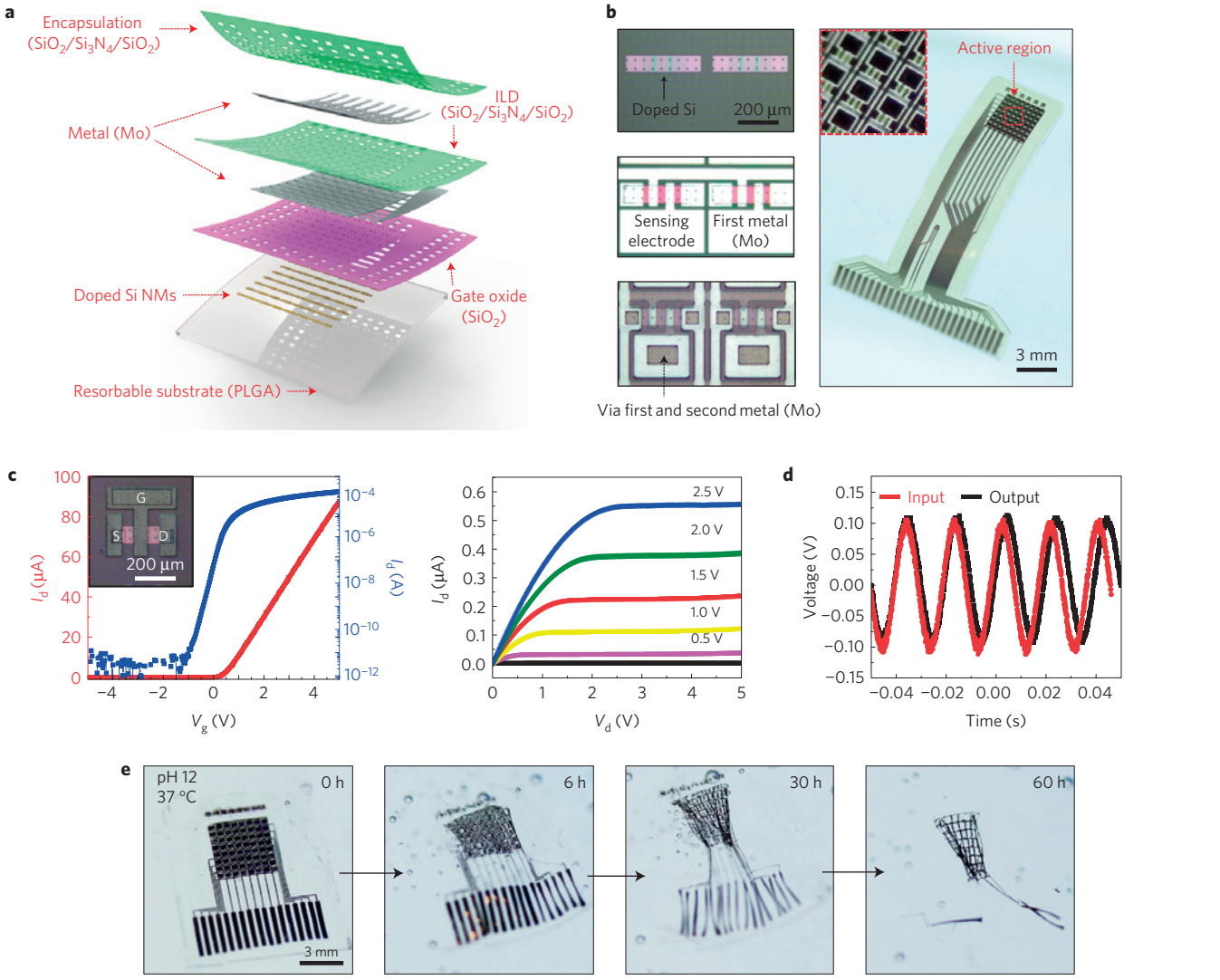

Figure 5 | Bioresorbable actively multiplexed neural electrode array. a, Schematic exploded-view illustration of an actively multiplexed sensing system for high-resolution ECoG, in a fully bioresorbable construction. This 8 × 8 embodiment includes 128 metal-oxide-semiconductor field-effect transistors (MOSFETs) where Si NMs serve as both the active semiconductor material and the neural interface electrodes. The metallization, the gate dielectric and the interlayer dielectric rely on thin films of Mo (~300 nm thick) and SiO_2 (~100 nm thick) and trilayers of SiO_2 (~300 nm thick)/Si_3N_4 (~400 nm thick)/SiO_2 (~300 nm thick), respectively. A second layer of Mo (~300 nm thick) defines column interface lines. A similar trilayer serves as the encapsulation. A film of poly(lactide-co-glycolide) (PLGA, ~30 μm thick) forms the substrate. **b**, Optical micrograph images of a pair of unit cells at various stages of fabrication (left) and a picture of a complete system (right). **c**, Left: linear (red) and log scale (blue) transfer curves for a representative n-channel MOSFET, for V_g swept from −5 to +5 V. The channel length (L_{ch}) and width (W) are 15 μm and 80 μm, respectively. The threshold voltage, mobility and on/off ratio are ~1 V, ~400 $cm^2 V^{-1} s^{-1}$ and ~10^8, respectively, with Mo for source, drain and gate electrodes, and SiO_2 for gate dielectrics. Right: Current–voltage characteristics, for V_g from 0 to 2.5 V with 0.5 V steps. **d**, Output response of a unit cell with respect to an input sine wave (200 mV peak to peak) on insertion in aqueous phosphate buffer solution (PBS, pH 7.4) at room temperature. **e**, Images collected at several stages of accelerated dissolution of a system immersed into an aqueous buffer solution (pH 12) at 37 °C.

post-implant (Fig. 4). In both control and bioresorbable devices, moderate subpial gliosis occurs at the implantation site, when compared to the control contralateral hemisphere. No significant astrogliosis is noted at distant sites within the ipsilateral hemisphere. Iba-1 immunohistochemistry demonstrates the presence of both resting ramified, as well as round activated microglia underneath the control electrode, which extends to the superficial layers I–III. In contrast, at the implantation site of the bioresorbable electrode, microglial cells show an almost exclusively ramified morphology. The contralateral side in both groups exhibits no microglial reaction. The sham-operated control demonstrates a similar moderate subpial gliosis, but with no change in microglial densities or morphology.

Actively multiplexed device designs enable high-resolution, high-channel-count neural interfaces by minimizing the number of wires needed for external data acquisition. In this context, Si NMs provide not only an excellent choice for the electrodes but also for the backplane electronics, including the necessary switching and buffer transistors as a scalable pathway towards systems with increased numbers of channels and area coverage. A fully bioresorbable design appears in Fig. 5a; a sequence of images at various stages of the fabrication appear on the right. This embodiment uses 128 n-channel metal-oxide-semiconductor field-effect transistors (MOSFETs), with molybdenum (Mo) for the source, drain and gate electrodes, and SiO_2 (~100 nm) for the gate dielectrics. Additional layers of Mo and a trilayer

© 2016 Macmillan Publishers Limited. All rights reserved

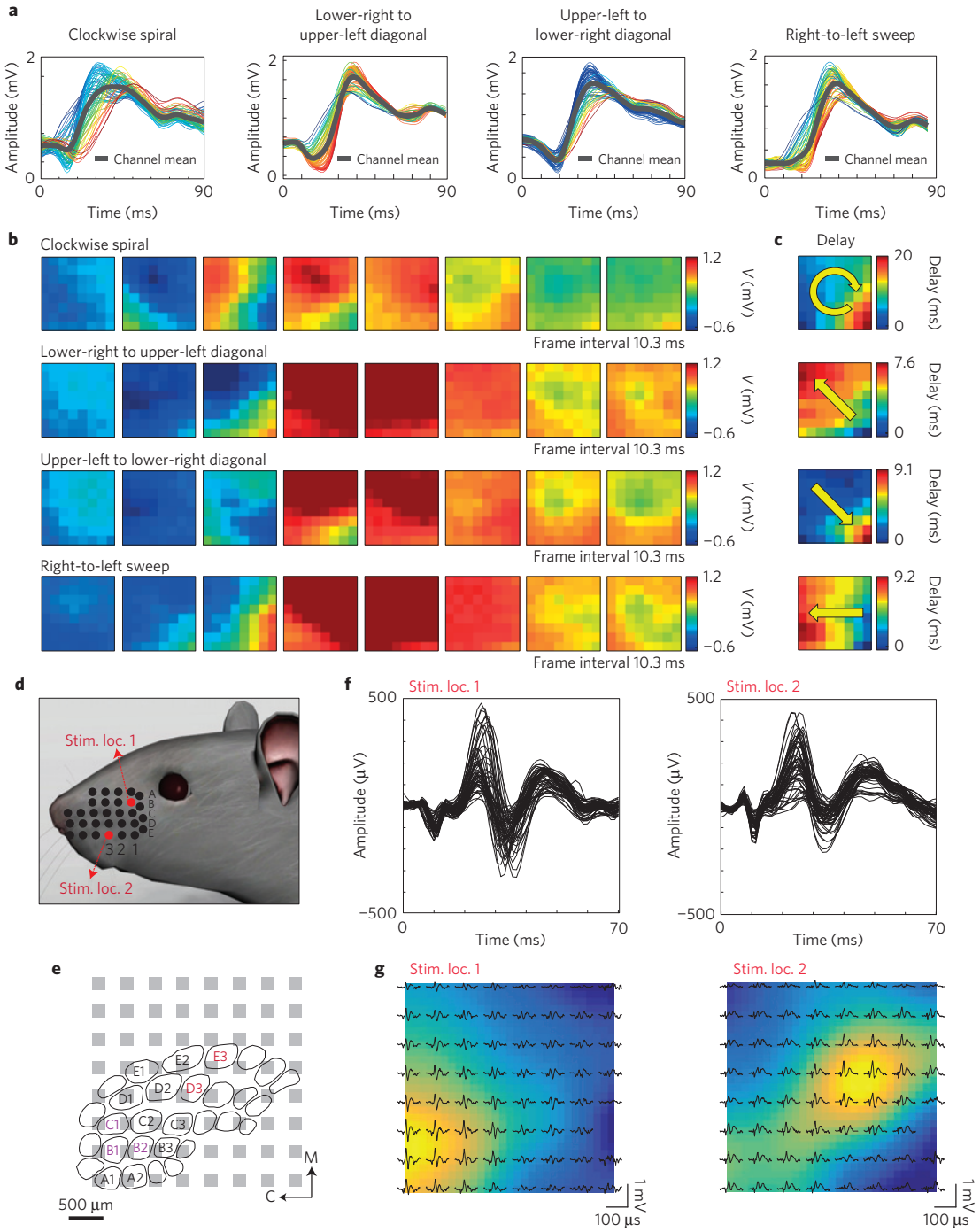

Figure 6 | Acute *in vivo* microscale electrocorticography (µECoG) with a 64-channel, bioresorbable, actively multiplexed array of measurement electrodes. a, Data recorded from picrotoxin-induced spikes (clockwise spiral, lower-right to upper-left diagonal, upper-left to lower-right diagonal and right-to-left sweep). The results correspond to measurements across the 64 channels of the array, and the average response (grey) from all channels. The waveforms are colour-coded according to the relative latency of the spike maximum (blue is earliest, red is latest). **b**, Movie frames corresponding to each spike pattern, showing the varied spatiotemporal µECoG voltage patterns from all 64 electrodes at the labelled time. Blue indicates negative, and dark red indicates the highest peak-to-peak voltage observed for each electrode site. The frame interval and colour scale are provided for each set of eight movie frames. **c**, Relative delay map for the bandpass filtered data of each spike activity from **b**, illustrating a clear phase singularity indicated by arrow. **d**, Illustration of the whisker stimulation locations (B1 and E3) in a rat model. **e**, Illustration of the barrel cortex and estimated relative location of the recording array based on evoked potential results. Visibly activated whiskers indicated by colour corresponding to the stimulation location. M, medial, C, caudal. **f**, Temporal characteristics of the potentials evoked by stimulation location 1 (left) and 2 (right). **g**, Spatial distribution of the potentials evoked by stimulation location 1 and 2. The colour map indicates the evoked potential size, interpolated across the array.

of SiO_2(~300 nm)/Si_3N_4 (~400 nm)/SiO_2 (~300 nm) form interconnects and interlayer dielectrics (ILD), respectively. A second layer of Mo (~300 nm) serves as column selects and additional sensing electrode pads. Another trilayer provides a blanket encapsulating layer that has openings only at the locations of the Mo interface electrodes. The amount of materials in a

© 2016 Macmillan Publishers Limited. All rights reserved

single device with active multiplexed addressing are 100 μg of Mo, 1.43 μg of Si, 306 μg of SiO_2, 264 μg of S_3iN_4, and 27 pg of P. For comparison, the daily intake limits, average daily intake values, and daily production of such materials appear in Supplementary Table 1. The chemistry, dissolution kinetics and biocompatibility of each of the constituent materials can be found elsewhere[39–46]. The lot and functional electrode yields are ∼10–20% and ∼80%, respectively. Failures arise from leakage currents associated with pinholes in the encapsulating layer, introduced by particulate contamination in our academic cleanroom facilities. Figure 5b presents photographs of a device, wrapped around a cylindrical tube, with an inset that shows arrays of active electrodes. Figure 5c summarizes the electrical properties of a representative n-type MOSFET, where the mobility and on/off ratio are ∼400 $cm^2 V^{-1}$ and ∼10^8, respectively, as calculated using standard field-effect transistor models. Figure 5d shows *in vitro* measurements on a representative unit cell. The output response was consistent with the input signal, thereby indicating proper operation. Details of *in vitro* experiments are in Supplementary Note 2 and Supplementary Figs 16–20.

Figure 5e shows a sequence of images during accelerated dissolution in PBS pH 12 at 37 °C. Si_3N_4 and Mo[40,41] dissolves in biofluids at pH 7.4 at 37 °C at a rate of ∼5.1 nm d^{-1} (Supplementary Fig. 8) and ∼16–25 nm d^{-1}, respectively. This system involves ∼1.3 μm, ∼800 nm, ∼300 nm, ∼600 nm and ∼30 μm thick layers of SiO_2, Si_3N_4, Si, Mo and PLGA, respectively. PLGA, Si and Mo in biofluids at 37 °C dissolve completely within in ∼4–6 weeks. Both SiO_2 and Si_3N_4, dissolve in six months under the same conditions. Supplementary Fig. 20 shows results of measurements of gain across the array and cumulative leakage current for a representative device immersed in PBS at pH 7.4. The average gain and yield were 94% and 100%, respectively.

Figure 6 provides details on *in vivo* recordings with a bioresorbable, multiplexed recording array. The leakage current is ∼10 nA. The 64-electrode array was placed on the cortical surface of the left hemisphere of an anaesthetized rat in a stereotaxic apparatus (Supplementary Fig. 21). Picrotoxin was applied topically to induce epileptiform activity, just before the placement of the array. The data reveal epileptic spikes and discharges that last ∼1–3 s (Supplementary Movie 1) and repeat every ∼10–15 s. A set of different epileptic spikes (clockwise spiral, lower-right to upper-left diagonal, upper-left to lower-right diagonal, and right-to-left sweep) is shown in Fig. 6a as representative recordings. The sequence of eight movie frames corresponding to each spike (Fig. 6b) clearly reveals the propagation of neural waves and associated spatiotemporally resolved patterns (Supplementary Movie 2–6). The delay maps represent the latency of the spike's peak at each site (Fig. 6c). Each spiking activity shows a distinctive spatial flow, indicated by the yellow arrow in each delay map. RMS power maps, corresponding to each representative spike (Fig. 6c and Supplementary Fig. 22), show the spatially resolved patterns.

In addition to epileptiform activity, spatial distributions of low-amplitude evoked cortical activity can be captured using the same device. Somatosensory evoked potential (SSEP) experiments were conducted in anaesthetized rats using the bioresorbable multiplexed array on the surface of the exposed barrel cortex. Evoked potentials were produced by stimulating two different whiskers (B1 and E3, Fig. 6d), corresponding to the barrel cortex and estimated relative location (Fig. 6e). The temporally resolved patterns of the evoked potentials are shown in Fig. 6f. The spatial distribution of the amplitude of the evoked potentials measured at the cortical surface by the array is consistent with the relative location of the activated whiskers on the barrel cortex as described with the colour map (Fig. 6g). These results collectively demonstrate an ability to record stimulus-evoked and drug-induced neural activity with high SNR. The same materials and device architectures can be easily adapted to larger areas and increased channel counts with potential for use in large-animal models and, in the future, for clinical monitoring applications.

The concepts introduced here form a robust foundation of capabilities in bioresorbable implantable electrode technology for various clinical problems, ranging from postoperation monitoring of brain activity to electrical monitoring of skeletal muscles or organ function. In all cases, the thin, flexible form factors minimize mechanical injury associated with implantation and chronic use. The use of Si as the active semiconductor material aligns the technology with the consumer electronics industry thereby suggesting a potential route to scale to higher densities of electrodes and larger areas.

Methods

Methods and any associated references are available in the online version of the paper.

Received 10 November 2015; accepted 14 March 2016; published online 18 April 2016

References

1. Niedermeyer, E. & da Silva, F. L. *Electroencephalography: Basic Principles, Clinical Applications, and Related Fields* (Lippincott Williams Wilkins, 2005).
2. Stacey, W. C. & Litt, B. Technology insight: neuroengineering and epilepsy—designing devices for seizure control. *Nature Clin. Pract. Neurol.* **4,** 190–201 (2008).
3. McKhann, G. M., Schoenfeld-McNeill, J., Born, D. E., Haglund, M. M. & Ojemann, G. A. Intraoperative hippocampal electrocorticography to predict the extent of hippocampal resection in temporal lobe epilepsy surgery. *J. Neurosurg.* **93,** 44–52 (2000).
4. Whitmer, D. *et al*. High frequency deep brain stimulation attenuates subthalamic and cortical rhythms in Parkinson's disease. *Front. Hum. Neurosci.* **6,** 155 (2012).
5. Litt, B. *et al*. Epileptic seizures may begin hours in advance of clinical onset: a report of five patients. *Neuron* **30,** 51–64 (2001).
6. Shapiro, M., Becske, T., Sahlein, D., Babb, J. & Nelson, P. K. Stent-supported aneurysm coiling: a literature survey of treatment and follow-up. *Am. J. Neuroradiol.* **33,** 159–163 (2012).
7. Wholey, M. H. *et al*. Global experience in cervical carotid artery stent placement. *Catheter. Cardio. Inter.* **50,** 160–167 (2000).
8. Frizzel, R. T. & Fisher, W. S. III Cure, morbidity, and mortality associated with embolization of brain arteriovenous malformations: a review of 1246 patients in 32 series over a 35-year period. *Neurosurgery* **37,** 1031–1040 (1995).
9. McNett, M. M. & Horowitz, D. A. International multidisciplinary consensus conference on multimodality monitoring: ICU processes of care. *Neurocrit. Care* **21,** 215–228 (2014).
10. Mayevsky, A., Manor, T., Meilin, S., Doron, A. & Ouaknine, G. E. Real-time multiparametric monitoring of the injured human cerebral cortex–a new approach. *Acta Neurochir. Suppl.* **71,** 78–81 (1998).
11. Khodagholy, D. *et al*. *In vivo* recordings of brain activity using organic transistors. *Nature Commun.* **4,** 1575 (2013).
12. Viventi, J. *et al*. Flexible, foldable, actively multiplexed, high-density electrode array for mapping brain activity *in vivo*. *Nature Neurosci.* **14,** 1599–1605 (2011).
13. Khodagholy, D. *et al*. NeuroGrid: recording action potentials from the surface of the brain. *Nature Neurosci.* **18,** 310–315 (2015).
14. Escabí, M. A. *et al*. A high-density, high-channel count, multiplexed μECoG array for auditory-cortex recordings. *J. Neurophysiol.* **112,** 1566–1583 (2014).
15. Qing, Q. *et al*. Nanowire transistor arrays for mapping neural circuits in acute brain slices. *Proc. Natl Acad. Sci. USA* **107,** 1882–1887 (2010).
16. Xiang, Z. *et al*. Ultra-thin flexible polyimide neural probe embedded in a dissolvable maltose-coated microneedle. *J. Micromech. Microeng.* **24,** 065015 (2014).
17. Tian, B. *et al*. Three-dimensional, flexible nanoscale field-effect transistors as localized bioprobes. *Science* **329,** 830–834 (2010).
18. Kozai, T. D. Y. *et al*. Ultrasmall implantable composite microelectrodes with bioactive surfaces for chronic neural interfaces. *Nature Mater.* **11,** 1065–1073 (2012).
19. Kuzum, D. *et al*. Transparent and flexible low noise graphene electrodes for simultaneous electrophysiology and neuroimaging. *Nature Commun.* **5,** 5259 (2014).
20. Vitale, F., Summerson, S. R., Aazhang, B., Kemere, C. & Pasquali, M. Neural stimulation and recording with bidirectional, soft carbon nanotube fiber microelectrodes. *ACS Nano* **9,** 4465–4474 (2015).

© 2016 Macmillan Publishers Limited. All rights reserved

21. Daube, J. & Rubin, D. *Clinical Neurophysiology* (Oxford Univ. Press, 2009).
22. King-Stephens, D. *et al*. Lateralization of mesial temporal lobe epilepsy with chronic ambulatory electrocorticography. *Epilepsia* **56,** 959–967 (2015).
23. Kang, S.-K. *et al*. Bioresorbable silicon electronic sensors for the brain. *Nature* **530,** 71–76 (2016).
24. Saha, R. *et al*. Highly doped polycrystalline silicon microelectrodes reduce noise in neuronal recordings *in vivo*. *IEEE Trans. Neural. Sys. Rehab. Eng.* **18,** 489–497 (2010).
25. Fontes, M. B. A. Electrodes for bio-application: recording and stimulation. *J. Phys. Conf. Ser.* **421,** 012019 (2013).
26. Oskam, G., Long, J. G., Natarajan, A. & Searson, P. C. Electrochemical deposition of metals onto silicon. *J. Phys. D* **31,** 1927–1949 (1998).
27. Zhang, X. G. *Electrochemistry of Silicon and its Oxide* (Kluwer Academic, 2001).
28. Schmickler, W. & Santos, E. *Interfacial Electrochemistry* Ch. 11 (Springer, 2010).
29. Morita, M., Ohmi, T., Hasegawa, E., Kawakami, M. & Ohwada, M. Growth of native oxide on a silicon surface. *J. Appl. Phys.* **68,** 1272–1281 (1990).
30. Seidel, H., Csepregi, L., Heuberger, A. & Baumgartel, H. Anisotropic etching of crystalline silicon in alkaline solutions: I. Orientation dependence and behavior of passivation layers. *J. Electrochem. Soc.* **137,** 3612–3626 (1990).
31. Gentile, P., Chiono, V., Carmagnola, I. & Hatton, P. V. An overview of poly(lactic-coglycolic) acid (PLGA)-based biomaterials for bone tissue engineering. *Int. J. Mol. Sci.* **15,** 3640–3659 (2014).
32. Shaw, F.-Z. Is spontaneous high-voltage rhythmic spike discharge in Long Evans rats an absence-like seizure activity? *J. Neurophysiol.* **91,** 63–77 (2004).
33. Pearce, P. S. *et al*. Spike–wave discharges in adult Sprague–Dawley rats and their implications for animal models of temporal lobe epilepsy. *Epilepsy Behav.* **32,** 121–131 (2014).
34. Rodgers, K. M., Dudek, F. E. & Barth, D. S. Progressive, seizure-like, spike-wave discharges are common in both injured and uninjured sprague-dawley rats: implications for the fluid percussion injury model of post-traumatic epilepsy. *J. Neurosci.* **35,** 9194–9204 (2015).
35. Polikov, V. S., Tresco, P. A. & Reichert, W. M. Response of brain tissue to chronically implanted neural electrodes. *J. Neurosci. Methods* **148,** 1–18 (2005).
36. Ryu, S. I. & Shenoy, K. V. Human cortical prostheses: lost in translation? *Neurosurg. Focus* **27,** E5 (2009).
37. Biran, R., Martin, D. C. & Tresco, P. A. Neuronal cell loss accompanies the brain tissue response to chronically implanted silicon microelectrode arrays. *Exp. Neurol.* **195,** 115–126 (2005).
38. Biran, R., Martin, D. C. & Tresco, P. A. The brain tissue response to implanted silicon microelectrode arrays is increased when the device is tethered to the skull. *J. Biomed. Mater. Res. A* **82,** 169–178 (2007).
39. Hwang, S.-W. *et al*. A physically transient form of silicon electronics. *Science* **337,** 1640–1644 (2012).
40. Yin, L. *et al*. Dissolvable metals for transient electronics. *Adv. Funct. Mater.* **24,** 645–658 (2014).
41. Badawy, W. A. & Al-Kharafi, F. M. Corrosion and passivation behaviors of molybdenum in aqueous solutions of different pH. *Electrochim. Acta* **44,** 693–702 (1998).
42. Kang, S. *et al*. Biodegradable thin metal foils and spin-on glass materials for transient electronics. *Adv. Funct. Mater.* **7,** 9297–9305 (2015).
43. Kang, S.-K. *et al*. Dissolution behaviors and applications of silicon oxides and nitrides in transient electronics. *Adv. Funct. Mater.* **24,** 4427–4434 (2014).
44. Hwang, S.-W. *et al*. Dissolution chemistry and biocompatibility of single-crystalline silicon nanomembranes and associated materials for transient electronics. *ACS Nano* **8,** 5843–5851 (2014).
45. Kue, R. *et al*. Enhanced proliferation and osteocalcin production by human osteoblast-like MG63 cells on silicon nitride ceramic discs. *Biomaterials* **20,** 1195–1201 (1999).
46. Bal, B. S. & Rahaman, M. N. Orthopedic applications of silicon nitride ceramics. *Acta Biomater.* **8,** 2889–2898 (2012).

Acknowledgements

The work was funded by the Defense Advanced Research Projects Agency, the Penn Medicine Neuroscience Center Pilot Grant, T32- Brain Injury Research Training Grant (5T32NS043126-12) and the Mirowski Family Foundation. Images in figures 2e, 3a and 6d from 3D Rat Anatomy Software (www.biosphera.org).

Author contributions

K.J.Y., D.K., B.L. and J.A.R. designed the research. K.J.Y., D.K., S.-W.H., B.H.K., N.H.K., S.M.W., K.C., H.F., K.J.S., H.N.L., S.-K.K., J.-H.K. and J.Y.L. fabricated the devices and electronics. K.J.Y., D.K., S.M.W., M. Trumpis, H.F., M. Thompson, H.B., M.A.D., T.L. and J.V. conceived and performed bench tests, and analysis. D.K., K.J.Y., H.J., A.G.R., M.A.D. and T.H.L. performed *in vivo* experiments and analysed the data. D.T. and F.E.J. performed biocompatibility and histology studies. H.C. and Y.H. performed mechanical simulations. K.J.Y., D.K., A.G.R., M.Trumpis, J.V., B.L. and J.A.R. wrote the manuscript.

Additional information

Supplementary information is available in the online version of the paper. Reprints and permissions information is available online at www.nature.com/reprints. Correspondence and requests for materials should be addressed to B.L. or J.A.R.

Competing financial interests

The authors declare no competing financial interests.

© 2016 Macmillan Publishers Limited. All rights reserved

Methods

Fabrication of passive electrode arrays. Fabrication of the passive electrode arrays began with solid-state phosphorus doping (PH-1000N Source, Saint Gobain, 1,000 °C for 10 min) of p-type device Si on a Si-on-insulator (SOI, top Si ~300 nm, SOITEC) wafer. Removing the buried oxide layer of the SOI by wet etching with concentrated HF released the device Si as a Si NM, retrieved with a slab of the elastomer poly(dimethylsiloxane) (PDMS) and transfer-printed to a spin-cast bilayer of poly(methylmethacrylate) (PMMA, ~800 nm thick) and polyimide (PI, ~300 nm thick) on a Si wafer. Photolithography and reactive ion etching (RIE) defined a pattern of electrodes and interconnects in the Si NMs. Plasma-enhanced chemical vapour deposition (PECVD) formed a layer of SiO_2 (thickness 100 nm) as encapsulation. Patterned etching with buffered oxide etchant removed the SiO_2 from the electrode regions. Spin casting and patterning a top coating of PI (~300 nm thick) placed the Si NM electrodes and interconnects near the neutral mechanical plane. Patterning a mesh structure across the multilayer (that is, PI, SIO_2, PI and PMMA) by RIE followed by immersion in buffered oxide etchant exposed the base layer of PMMA to allow its dissolution in acetone. Retrieval onto a slab of PDMS enabled removal of the bottom exposed layer of PI by RIE. Transfer onto a film of PLGA (~30 μm thick), facilitated by heating to temperatures close to the glass transition of the PLGA (55–60 °C, lactide/glycolide ratio of 75:25 composition), followed by elimination of the top layer of PI by RIE, completed the fabrication. Bonding an ACF cable to the terminal regions of the Si NM interconnects yielded connection points for interfaces to external data acquisition (DAQ) systems.

Fabrication of actively multiplexed electrode arrays. Fabrication began with growth of 200 nm of thermal oxide on a p-type SOI wafer (top Si ~320 nm, SOITEC), photolithography and immersion in buffered oxide etchant to create a mask for solid-state phosphorus diffusion (1,000 °C for 6 min) to define the source and drain contacts. Releasing, retrieving and transferring the doped Si NMs onto a temporary substrate, consisting of Si wafer with a bilayer coating of PI/PMMA, followed procedures similar to those described for passive electrode arrays. Photolithography and RIE etching patterned the Si NMs into geometries for an 8 × 8 array of unit cells, each consisting of two transistors connected in series for purpose of actively multiplexed readout. A thin layer of SiO_2 (PECVD at 220 °C, thickness ~100 nm) served as the gate dielectric. Buffered oxide etching through a photolithographically patterned mask formed openings through the SiO_2 to expose the source and drain contact regions. Photolithography and lift-off in acetone defined a patterned layer of Mo (sputter deposited, thickness ~300 nm) for the gate electrodes and metal interconnects. Deposition of a trilayer of SiO_2 (~300 nm)/Si_3N_4 (~400 nm)/SiO_2 (~300 nm) by PECVD formed the interlayer dielectric. Photolithography and buffered oxide etching created vertical interconnect access (via) holes for electrical connections between layers. An additional layer of Mo (thickness ~300 nm) patterned by photolithography and lift-off defined column select lines. Another trilayer of SiO_2 (~300 nm)/Si_3N_4 (~400 nm)/SiO_2 (~300 nm) served as encapsulation, with openings at the locations of the sensing electrodes and peripheral contact pads for interfacing to an external DAQ system. A spin-cast layer of PI served as device passivation. Selective RIE and buffered oxide etching through these multilayer stacks (diluted PI/trilayers of inorganic materials/trilayers of inorganic materials/Diluted PI) formed mesh structures that enabled release of active layers from the temporary substrate by dissolving the PMMA layer in acetone. Transfer printing steps followed, according to procedures similar to those for the passive electrode fabrication.

***In vivo* acute recordings of epileptiform activity.** The *in vivo* data Fig. 2 is representative of four different acute experiments, each of which lasted 5–6 h. The procedures, which were approved by the Institutional Care and Use Committee of the University of Pennsylvania, involved an anaesthetized rat with its head fixed in a stereotaxic apparatus. Wild-type, adult Long Evans male and female rats were used. The animal was anaesthetized with initially ketamine/xylazine and then isoflurane throughout the craniotomy and neural recordings. A craniotomy exposed a 4 × 8 mm region of cortex in either the left or right, or in both hemispheres. All recordings were taken in reference to a distant stainless steel bone screw inserted through the skull during the surgery. A commercial stainless steel microwire electrode (~100 um stainless steel wire from California Fine Wire) placed at 0.5 mm depth from the cortical surface in close proximity to the bioresorbable electrodes served as a control during acute recordings. Neural data was acquired by a FHC multichannel neural amplifier (FHC) and an acquisition system (16-bit Axon Instruments Digidata 1322A, Axon Instruments). Recordings were high-pass-filtered at 0.1 Hz. Neural recording data were analysed offline using Clampfit software (Axon Instruments) and custom Matlab software for neural signal analysis.

***In vivo* acute recordings of evoked responses by whisker stimulation.** The following procedures were approved by the Institutional Care and Use Committee of the University of Pennsylvania. One 150 g, Sprague-Dawley rat was anaesthetized with a ketamine (60 mg kg^{-1}), dexdomitor (0.25 mg kg^{-1}) solution and placed in a stereotaxic frame. A craniotomy was performed to expose the right barrel cortex. A skull screw was placed in the left frontal bone to serve as the reference electrode for the recordings. The recording array was placed over the exposed cortical surface. A pair of needle stimulating electrodes were inserted into the left mystacial pad at various locations. Brief electrical currents (~250–600 μA, 1 ms/phase, biphasic pulse) were passed between the electrodes to activate the intrinsic muscles of the vibrissae, causing a visible protraction of the whiskers. Current amplitude and electrode spacing was adjusted for focal activation, usually 1–4 whiskers. Cortical potentials evoked by the whisker stimulation were recorded at 781.25 samples s^{-1}.

***In vivo* chronic recordings.** An adult Long Evans rat was anaesthetized with isoflurane and placed in a stereotactic frame (David Kopf Instruments). Body temperature was maintained with a heating blanket and the eyes were covered with ointment to prevent drying. The skull was exposed and a large craniotomy (4 × 8 mm^2) was made between bregma and lambda and laterally to the midline. The electrode was placed on the exposed dura and a slurry of gelfoam and saline was layered on top of the electrode. A screw electrode was placed contralaterally to the experimental array, with another such electrode placed posterior to lambda as a ground and reference. Additional screws were secured in the skull for anchoring. The skull and electrodes were then covered with dental cement and the connecting plug was secured on top. The rat was given meloxicam for postoperative pain and allowed to recover on a heating pad. The rat was given meloxicam daily for three days after surgery to minimize pain. After one week the animal was placed in a cage for video/EEG recording. EEG signals were collected continuously from three channels on the array and from the screw. The signals were amplified and low-pass-filtered at 600 Hz (Multichannel Systems) and sampled at 2,000 Hz with a 16-bit digitizer (National Instruments). Data was acquired using a custom written MATLAB routine.

Chronic evaluation of immunohistochemistry. Rats ($n = 14$) were anaesthetized and transcardiac perfusion was performed using phosphate-buffered saline (PBS 10x, cat. # BM-220, Boston BioProducts), followed by 4% paraformaldehyde (PFA, cat. # BM-155, Boston BioProducts). Whole brains were then removed and post-fixed overnight at 4 °C in the same 4% PFA solution. Subsequently, fixed brains were cryoprotected in 30% sucrose (cat. # 57-50-1, Sigma-Aldrich) at 4 °C and coronal sections were cut at 20 μm using a Leica CM3050 S cryostat (Leica Biosystems). Serial sections, spanning the entire craniotomy site, were mounted on charged slides and stored at −20 °C until use. For immunostaining, slides were first immersed in an antigen retrieval solution (0.1 M citrate buffer, pH 6.0, cat# ab64214, Abcam) and placed in a water bath at 95 °C for 10 min. After cooling, sections were rinsed in distilled water, incubated in a blocking solution containing 0.1% Triton X-100 (cat. # 9002-93-1, Sigma-Aldrich) and 5% normal goat serum (cat. # GS-0500, Equitech-Bio) for one hour at room temperature (RT) and then incubated overnight at 4 °C with the following primary antibodies: anti- Glial Fibrillary Acidic Protein (GFAP, 1:1,000, cat. # SMI-22R, Covance), and anti-ionized calcium-binding adapter molecule 1 (Iba-1, 1:1,000, cat. # 019-19741, Wako Chemicals USA). After 3×20 min washes in PBS, sections were incubated with the corresponding fluorescent secondary antibodies (Alexa Fluor 488 goat anti-mouse IgG2b, 1:1,000, cat. # A-21141, and Alexa Fluor 568 goat anti-rabbit IgG, 1:1,000, cat. # A-11011, Invitrogen by Life Technologies). After the final washes (3 × 20 min in PBS), the slides were cover-slipped with an anti-fade medium containing the nuclear stain DAPI (Fluoromount-G+DAPI, cat. # 0100-20, Southern Biotechnology). Control sections were incubated with omission of one or both primary antibodies, adding only the secondary antibodies to exclude false-positive labelling. Slides were examined on an epifluorescence microscope (Zeiss Axioscope) and images were acquired with a 20× objective and a Spot RT3 digital camera, using the Spot Software 5.1 (Diagnostic Instruments). Digital images were processed using Adobe Photoshop 12.0 (Adobe Systems).

© 2016 Macmillan Publishers Limited. All rights reserved

nature materials

SUPPLEMENTARY INFORMATION

DOI: 10.1038/NMAT4624

Bioresorbable silicon electronics for transient spatiotemporal mapping of electrical activity from the cerebral cortex

Ki Jun Yu[1,2†], Duygu Kuzum[3,4,5†], Suk-Won Hwang[6], Bong Hoon Kim[2,7], Halvor Juul[8], Nam Heon Kim[2,7], Sang Min Won[1,2], Ken Chiang[9], Michael Trumpis[9], Andrew G. Richardson[4,10], Huanyu Cheng[11], Hui Fang[2,7], Marissa Thomson[3,4,12], Hank Bink[3,4], Delia Talos[8], Kyung Jin Seo[2,7], Hee Nam Lee[2,13], Seung-Kyun Kang[2,7], Jae-Hwan Kim[2,7], Jung Yup Lee[2,13], Younggang Huang[14], Frances E. Jensen[4,8], Marc A. Dichter[4,8], Timothy H. Lucas[4,10], Jonathan Viventi[9], Brian Litt [3,4,8*], John A. Rogers[1,2,7,*]

[1] *Department of Electrical and Computer Engineering, University of Illinois at Urbana-Champaign, Urbana, IL 61801, USA*

[2] *Frederick Seitz Materials Research Laboratory, University of Illinois at Urbana-Champaign, Urbana, IL 61801, USA*

[3] *Department of Bioengineering, University of Pennsylvania, Philadelphia, Pennsylvania 19104, USA*

[4] *Center for Neuroengineering and Therapeutics, University of Pennsylvania, Philadelphia, PA 19104, USA*

[5] *Department of Electrical and Computer Engineering, University of California, San Diego, San Diego, CA 92093*

[6] *KU-KIST Graduate School of Converging Science and Technology, Korea University, Seoul 136-701, Republic of Korea*

[7] *Department of Materials Science and Engineering, University of Illinois at Urbana-Champaign, Urbana, IL 61801, USA*

[8] *Department of Neurology, Perelman School of Medicine, University of Pennsylvania, Philadelphia, PA 19104, USA*

[9] *Department of Biomedical Engineering, Duke University, Durham, NC 27708, USA*

[10] *Department of Neurosurgery, Perelman School of Medicine, University of Pennsylvania, Philadelphia, PA 19104, USA.*

[11] *Department of Engineering Science and Mechanics, Penn State University, University Park, PA 16802, USA.*

[12] *Department of Chemical and Biomolecular Engineering University of Pennsylvania, Philadelphia, Pennsylvania 19104, USA*

© 2016 Macmillan Publishers Limited. All rights reserved.

[13] *Department of Chemical and Biomolecular Engineering, University of Illinois at Urbana-Champaign, Urbana, IL 61801, USA*

[14] *Department of Mechanical Engineering and Department of Civil and Environmental Engineering, Northwestern University, Evanston, IL 60208, USA*

[†]*These authors are contributed equally to this work.*
**To whom correspondence should be addressed. E-mail: jrogers@illinois.edu or littb@upenn.edu*

© 2016 Macmillan Publishers Limited. All rights reserved.

Supplementary Note 1: *In vitro* experiments of phosphorus doped Si NM electrodes

Results of impedance measured on devices constructed using Si NMs with different dopant species and concentrations (phosphorus, between ~10^{17} and ~10^{20}/cm^3; and boron, at ~10^{20}/cm^3) are comparable at all frequencies, up to ~1 kHz. (Supplementary Figs 4 and 5). The impedances measured from Si NMs with different thicknesses across a relevant range also show similar values (Supplementary Fig. 6), thereby suggesting an ability for continuous, reliable neural recording even as the electrodes dissolve over time. The doping level and the thickness do, however, strongly affect the time for complete dissolution, where increasing the level and thickness increases the lifetime. The impedance decreases, as expected, inversely with the areas of the electrodes (phosphorous, ~10^{20}/cm^3), as illustrated in the data of Supplementary Fig. 7 for dimensions of 200×200 μm^2 (A1), 300×300 μm^2 (A2), 400×400 μm^2 (A3), 500×500 μm^2 (A4).

Supplementary Note 2: Operation of the multiplexing on a representative unit cell

Supplementary Figs 16-18 summarize the key aspects of the designs of circuits that incorporate these transistors for multiplexed addressing. The approach involves two transistors per unit cell[12,14], in which a buffer transistor connects to the interface electrode to provide buffering of measured biopotentials, and a multiplexing transistor allows electrodes in a given column to share a single output wire. The surface electrodes appear in the top layer, where they come into physical contact with the brain; they connect to the underlying backplane circuit through vertical interconnect access holes (vias). An active shielding scheme described in Supplementary Fig. 18 improves the signal to noise ratio of the system by reducing the parasitic capacitance and increases the gain of each site of the electrodes. The operation involved successive application of 3V (V_r) to

© 2016 Macmillan Publishers Limited. All rights reserved.

the gate of the multiplexing transistor when a particular row was activated and -3V (V_r) when the row was not selected (Supplementary Figs 16 and 17). A constant current of 4 μA was used to bias the column output and complete the source follower amplifier. The output voltage (V_c) was high-pass filtered to have an average DC bias of 2V and connected to the column power source line (V_{as}). By using analog feedback, the negative effects of parasitic capacitance in the drain of the buffer transistor are reduced and the AC signal gain of the electrode array is improved. A 50 Hz, 200 mV (peak to peak) sinusoidal waveform was applied to a metal reference electrode immersed in PBS at pH 7.4 and recorded from the active electrode array (Supplementary Fig. 19). During multiplexed sampling, driving the row select signal selects a single row of electrodes at a time. This scheme allows the unit cells in the corresponding row to drive the column output lines which connect to a high-speed analog to digital converter. Row select signals are rapidly cycled to sample all electrodes on the array. The entire device connects to an external data acquisition (DAQ) system through a zero insertion force (ZIF) connector with 26 contact.

© 2016 Macmillan Publishers Limited. All rights reserved.

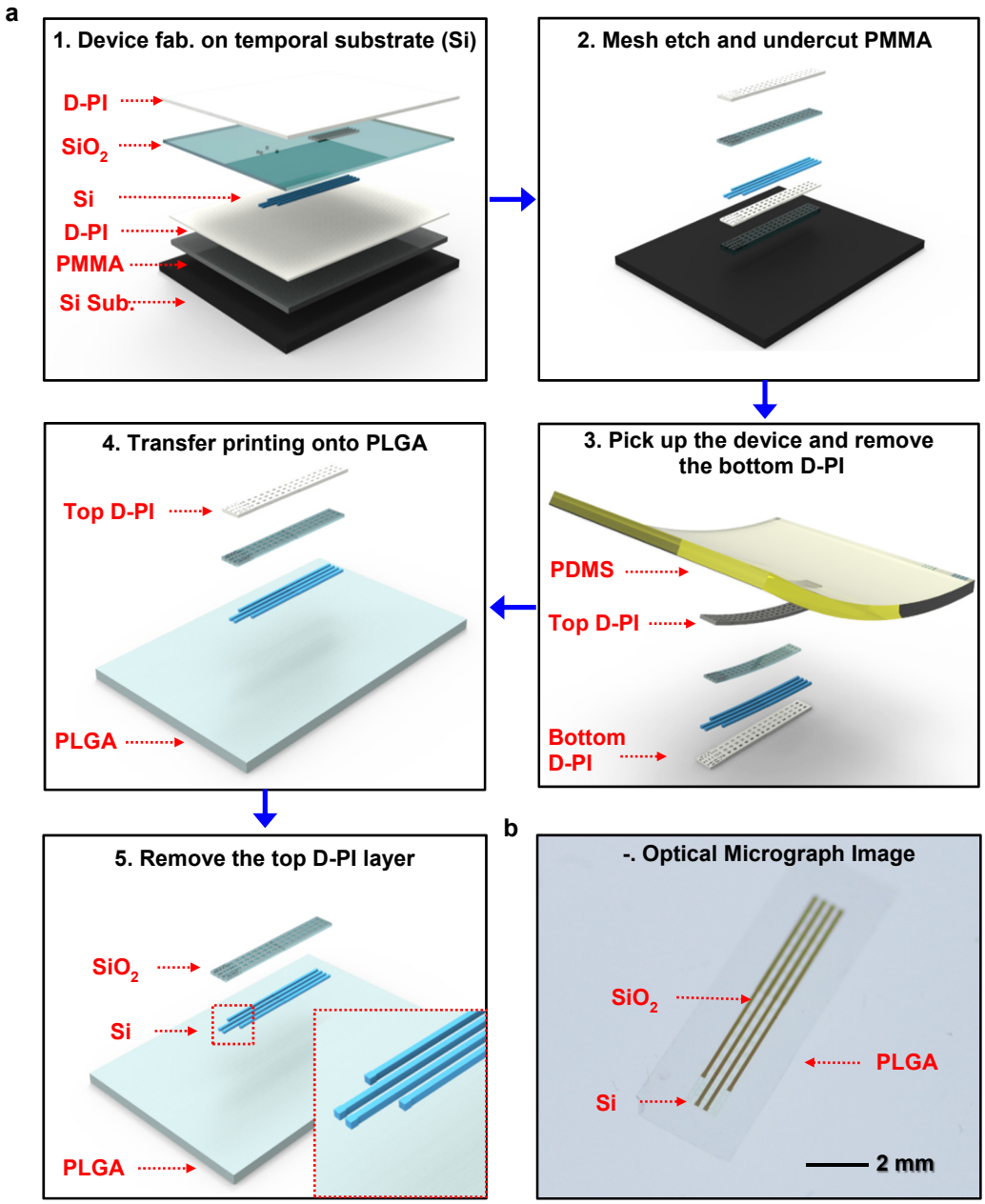

Supplementary Figure S1 | Materials and procedures for fabricating bioresorbable passive electrodes on biodegradable substrates (PLGA) and a device image. (a) Schematic illustrations of key processes for fabricating bioresorbable passive electrodes: (1) printing highly n-doped Si on temporary substrates, (2) defining the mesh structure, followed etching by RIE and immersion buffered oxide etchant (BOE), (3) retrieving the device onto a PDMS slab, (4) printing the device onto a bioresorbable substrate (PLGA), and (5) removing the top D-PI layer. (b) Optical image of a complete device.

© 2016 Macmillan Publishers Limited. All rights reserved.

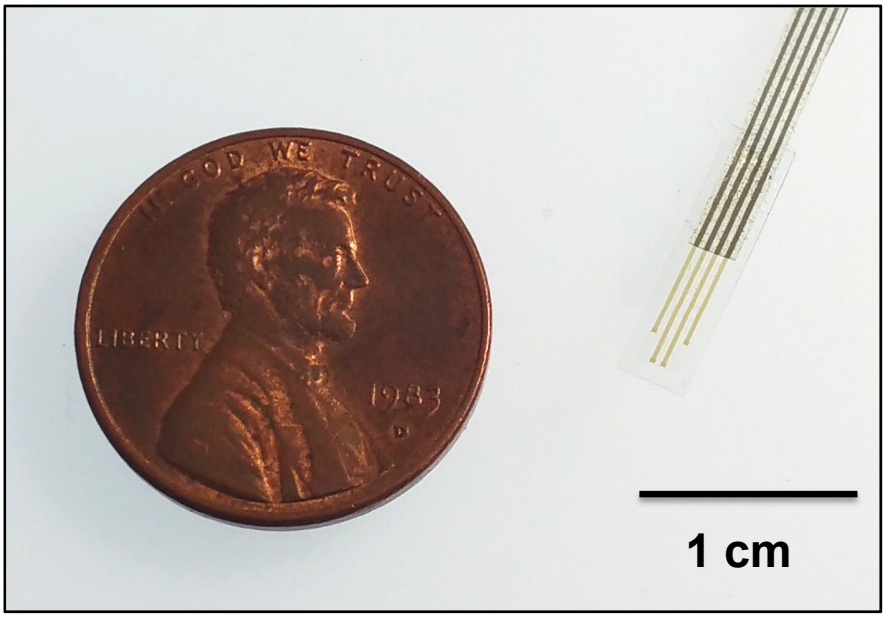

Supplementary Figure S2 | A photograph of a bioresorbable passive electrode array with a penny.

© 2016 Macmillan Publishers Limited. All rights reserved.

a

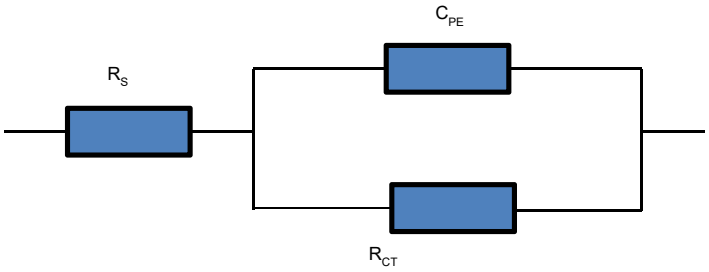

b

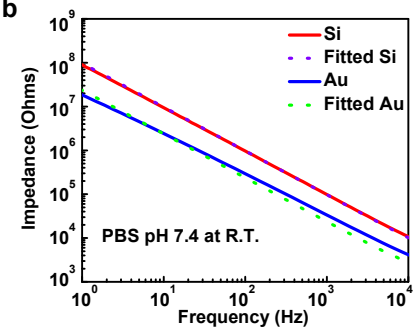

c

	C_{PE}	R_{CT}
Si	2.5 μF/cm^2	4 G-ohms
Au	10 μF/cm^2	0.3 G-ohms

Supplementary Figure S3 | EIS characterization of Si and Au. (a) Schematic description of the equivalent circuit model used to fit EIS measurement results. C_{PE} is the constant phase element representing the double-layer capacitance; R_{CT} is the charge transfer resistance; and R_S is the solution resistance. (b) Results of measurement (solid lines) and fitting (dashed lines) for the impedance. (c) Representative values of C_{PE} and R_{CT} for Au and Si.

© 2016 Macmillan Publishers Limited. All rights reserved.

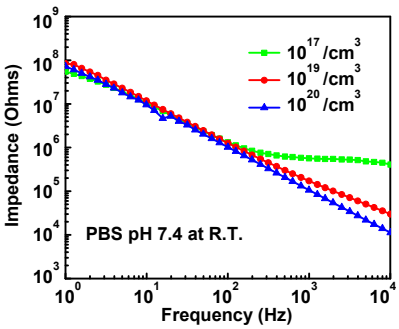

Supplementary Figure S4 | Impedance spectra of phosphorus doped Si NM electrodes with different doping concentrations (10^{17} /cm^3, 10^{19} /cm^3, 10^{20} /cm^3).

© 2016 Macmillan Publishers Limited. All rights reserved.

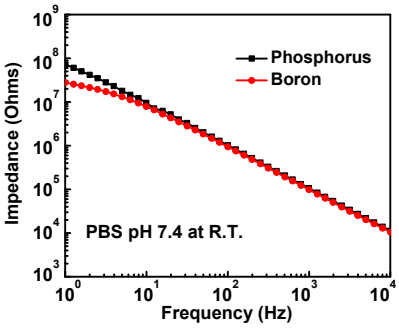

Supplementary Figure S5 | Impedance spectra of boron and phosphorus doped Si NM electrodes with the same doping concentrations (10^{20} /cm^3) for both boron and phosphorus.

© 2016 Macmillan Publishers Limited. All rights reserved.

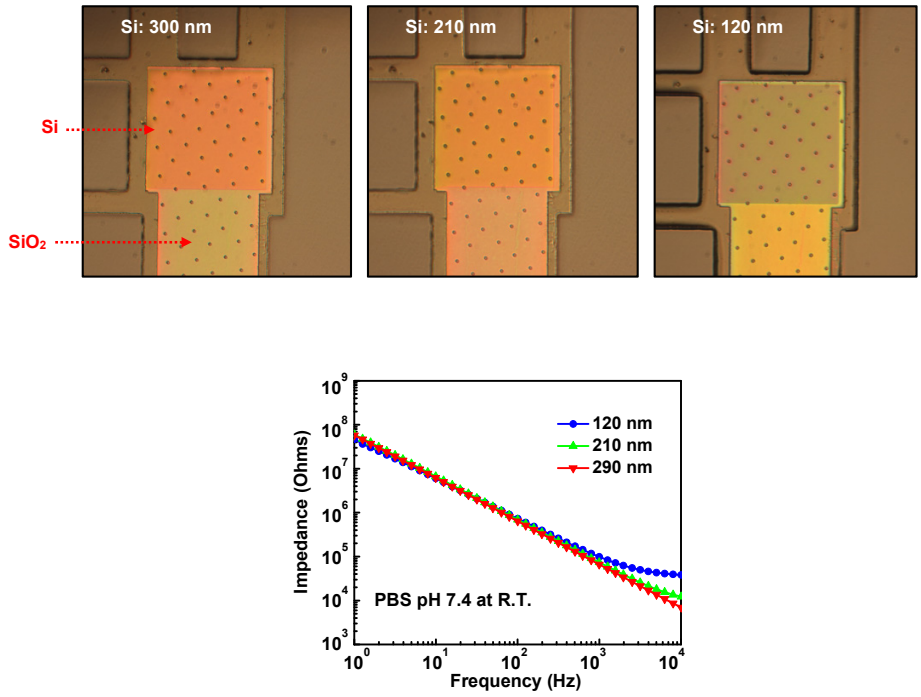

Supplementary Figure S6 | Impedance spectra of different thicknesses (300 nm, 210 nm, 120 nm) of sites of Si.

© 2016 Macmillan Publishers Limited. All rights reserved.

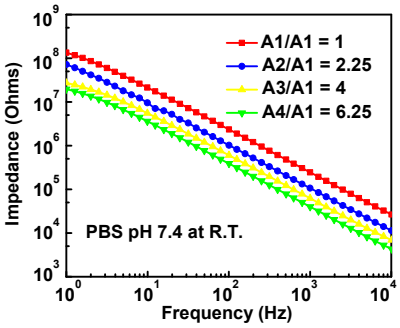

Supplementary Figure S7 | Impedance spectra of phosphorus doped Si NM electrodes with the different areas (200×200 μm^2 (A1), 300×300 μm^2 (A2), 400×400 μm^2 (A3), 500×500 μm^2 (A4)) of sites.

© 2016 Macmillan Publishers Limited. All rights reserved.

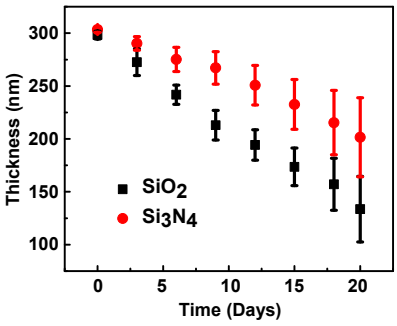

Supplementary Figure S8 | Hydrolysis kinetics for SiO_2 and Si_3N_4 used in the devices. Thicknesses as a function of time during dissolution in artificial cerebrospinal fluid (ACSF) at 37 °C. The initial thicknesses were 300 nm for both SiO_2 and Si_3N_4.

© 2016 Macmillan Publishers Limited. All rights reserved.

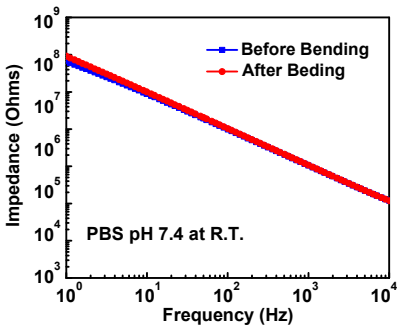

Supplementary Figure S9 | Impedance spectra of before and after bending with 2 mm bending radius of a bioresorbable passive electrode array.

© 2016 Macmillan Publishers Limited. All rights reserved.

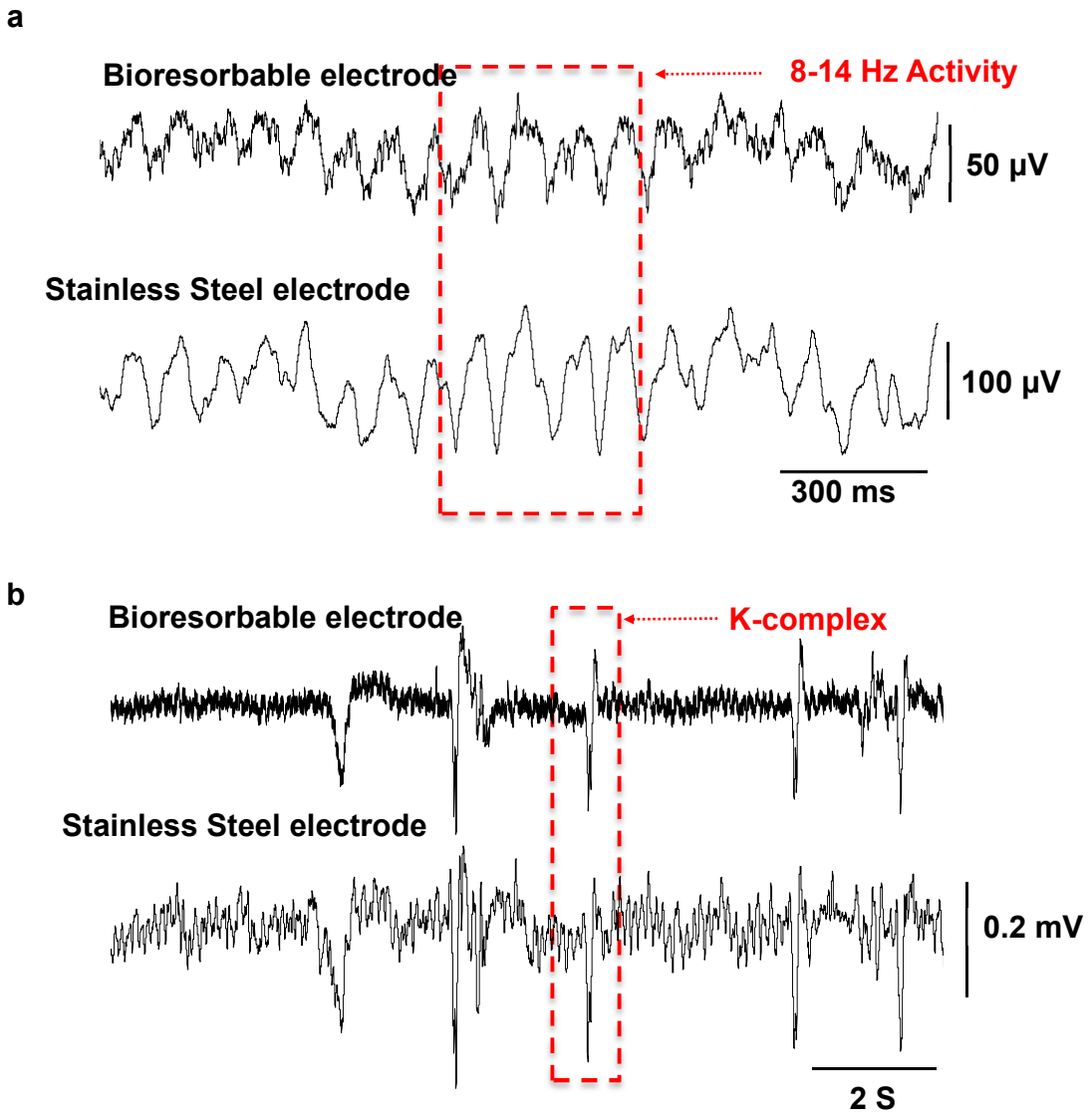

Supplementary Figure S10 | *In vivo* neural recordings in rats. (a) Slow wave activity and (b) k-complexes recorded using a bioresorbable electrode array and a control stainless steel microwire electrode.

© 2016 Macmillan Publishers Limited. All rights reserved.

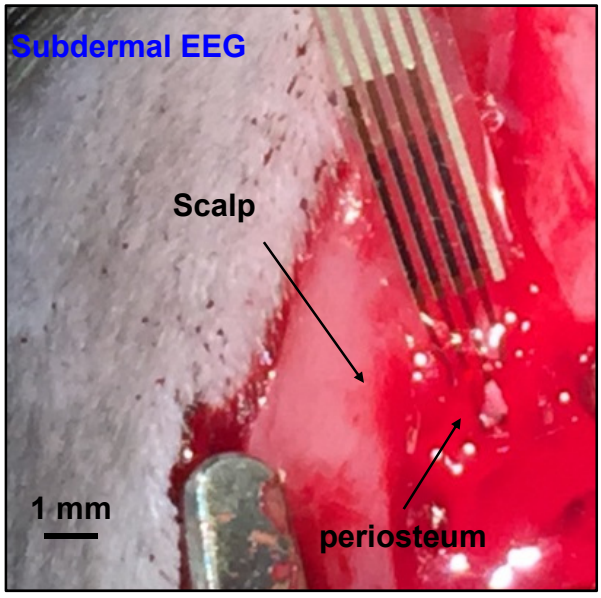

Supplementary Figure S11 | A photograph of bioresorbable passive electrode array placed onto the periosteum of a rat.

© 2016 Macmillan Publishers Limited. All rights reserved.

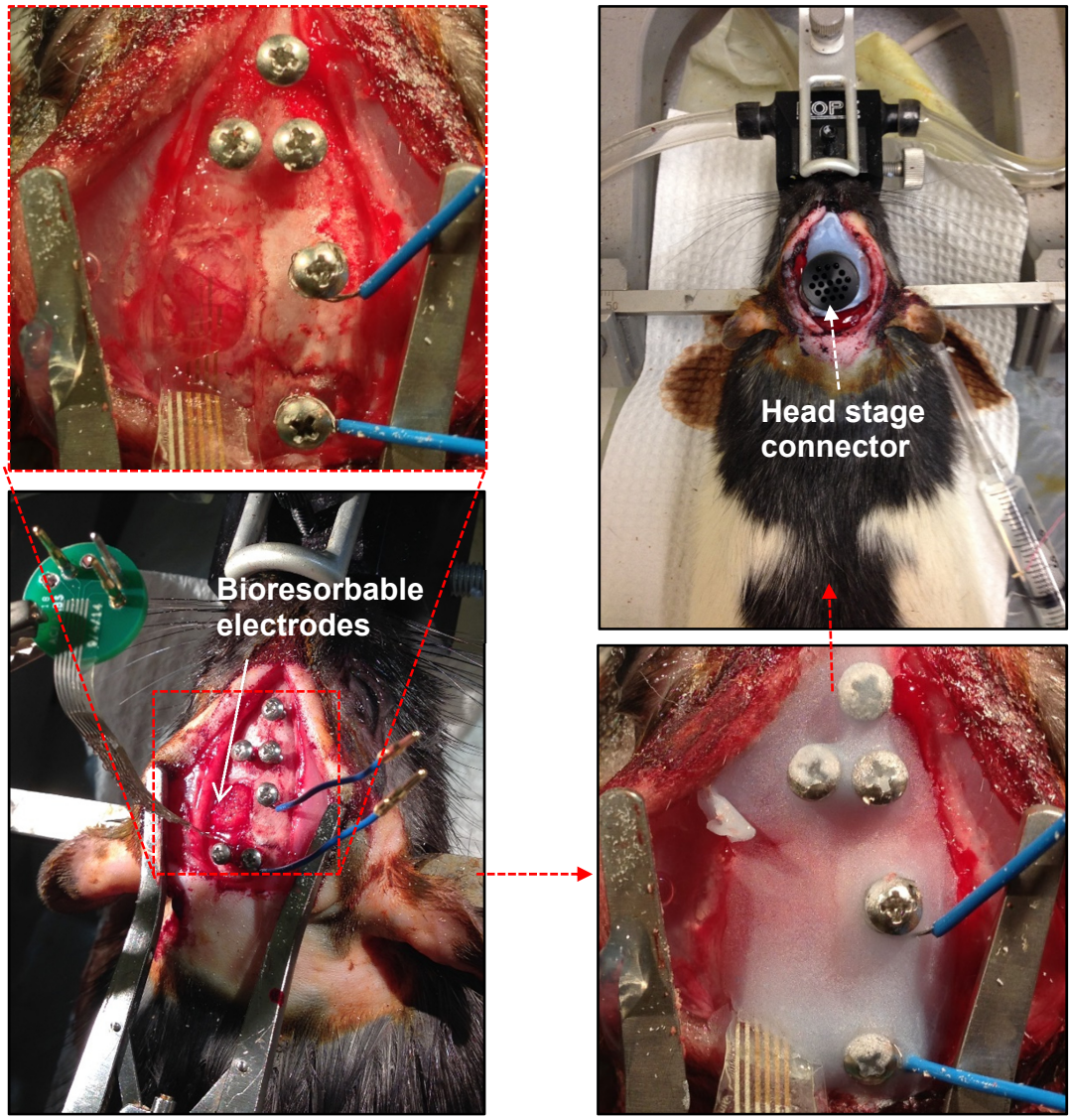

Supplementary Figure S12 | Photographs of surgery associated with chronic recording experiments. Implanting the bioresorbable electrode arrays on a rat brain, applying the dental cement, and then burying the head stage board.

© 2016 Macmillan Publishers Limited. All rights reserved.

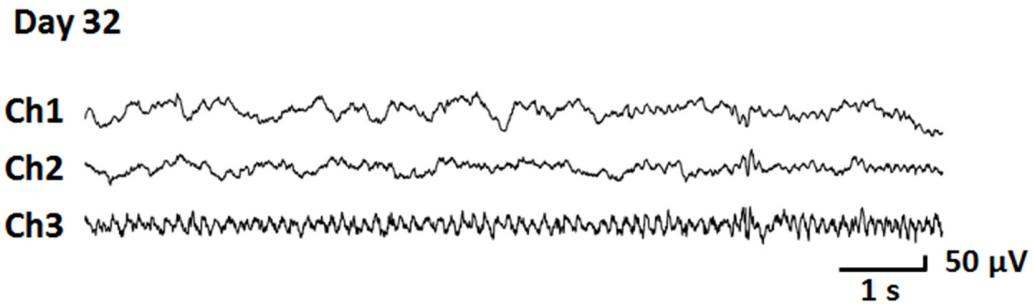

Supplementary Figure S13 | Representative ECoG signals recorded by the bioresorbable array (Ch1, Ch2, and Ch3) and the control electrode on day 32.

© 2016 Macmillan Publishers Limited. All rights reserved.

Supplementary Figure S14 | A photograph after the surgery of the device implantation, showing freely moving rat with a head stage connector.

© 2016 Macmillan Publishers Limited. All rights reserved.

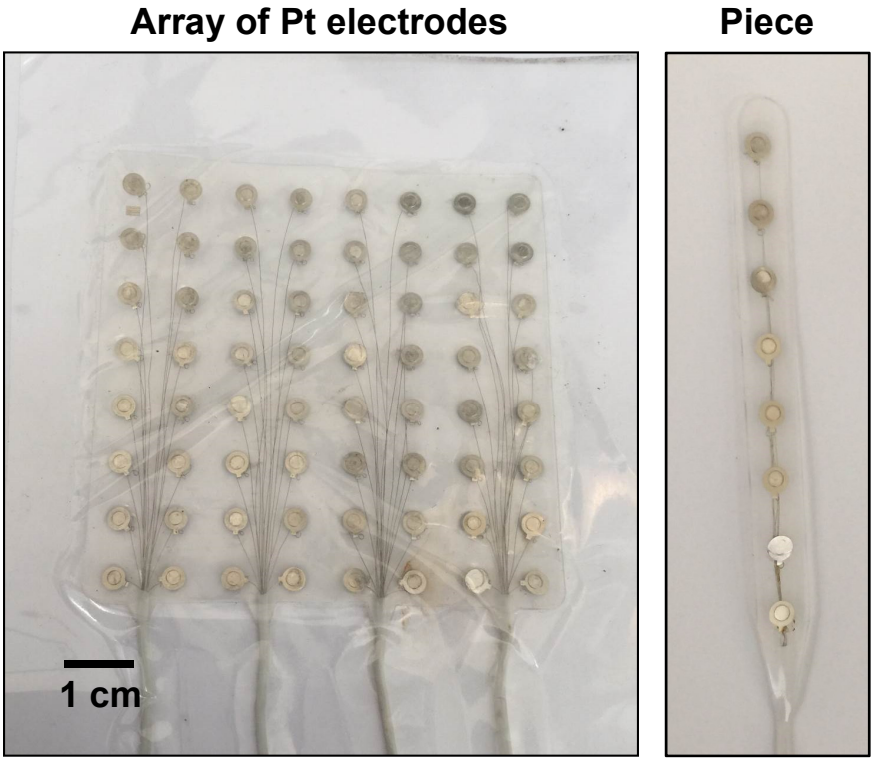

Supplementary Figure S15 | Clinical platinum electrodes for ECoG, 8 × 8 Electrode Grid (left), and 1 × 8 Strip Electrode (right).

© 2016 Macmillan Publishers Limited. All rights reserved.

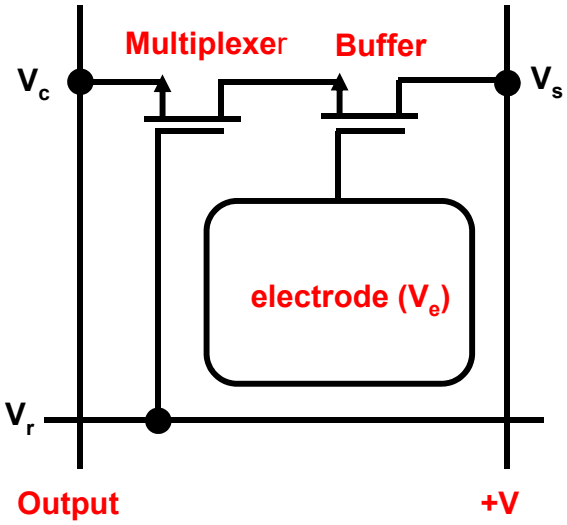

Supplementary Figure S16 | Schematic circuit diagram of a single unit cell containing two matched n-MOS transistors in an actively multiplexed, bioresorbable electrode array.

© 2016 Macmillan Publishers Limited. All rights reserved.

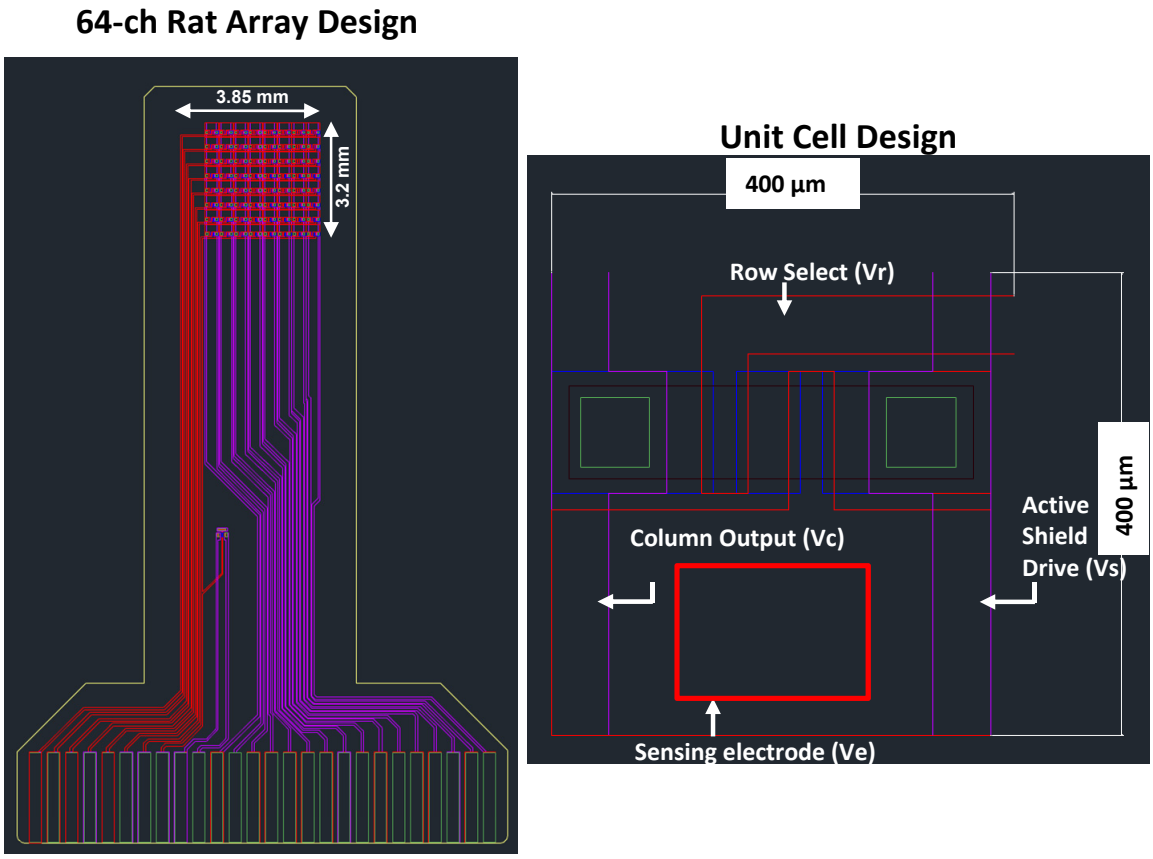

Supplementary Figure S17 | Schematic illustration of a 8×8 array of actively multiplexed channels, showing the entire device (left), and the unit cell design (right).

© 2016 Macmillan Publishers Limited. All rights reserved.

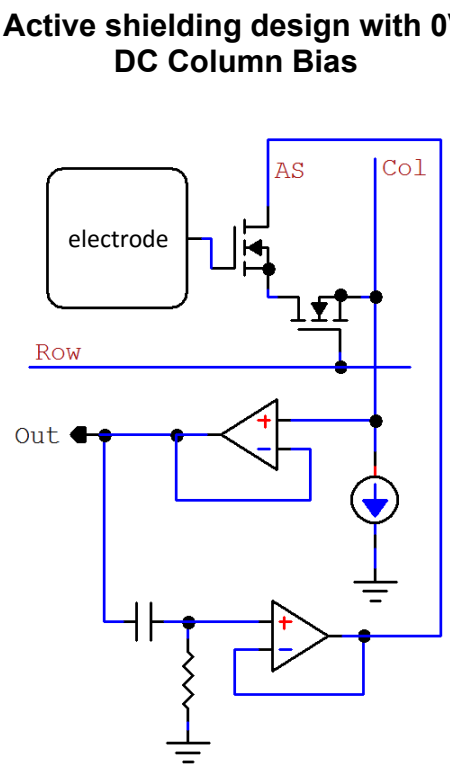

Supplementary Figure S18 | Schematic circuit diagram for an active shielding circuit for the actively multiplexed array.

© 2016 Macmillan Publishers Limited. All rights reserved.

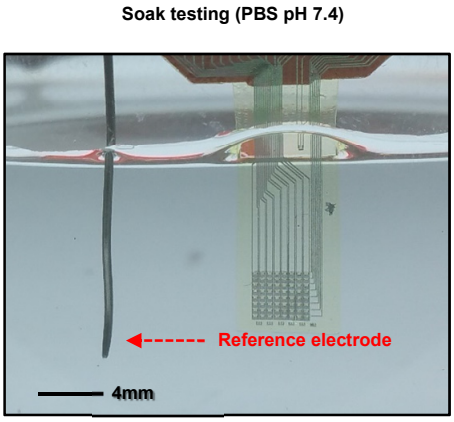

Supplementary Figure S19 | *In vitro* test setup for actively multiplexed array.

© 2016 Macmillan Publishers Limited. All rights reserved.

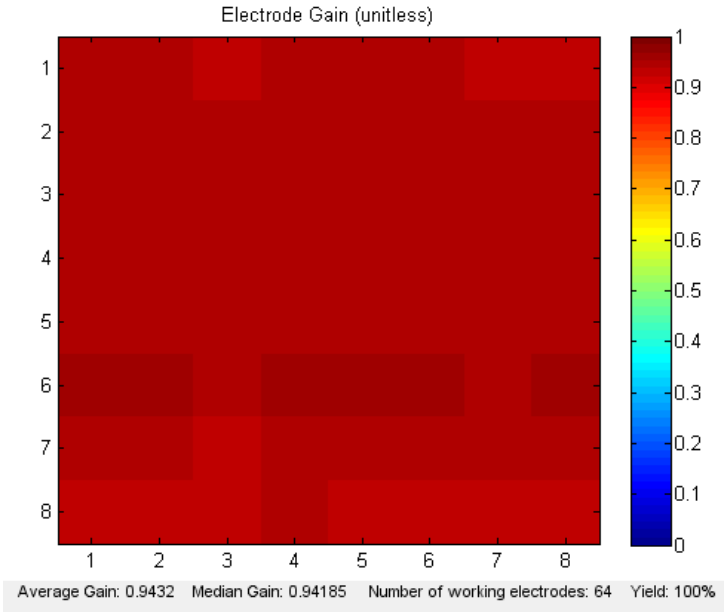

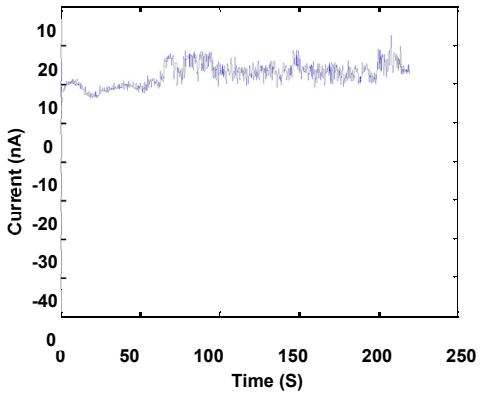

Supplementary Figure S20 | Color map illustrating the spatial distribution of the electrode response, demonstrating the spatial uniformity of the gain of an actively multiplexed, bioresorbable electrode array and leakage current over time.

© 2016 Macmillan Publishers Limited. All rights reserved.

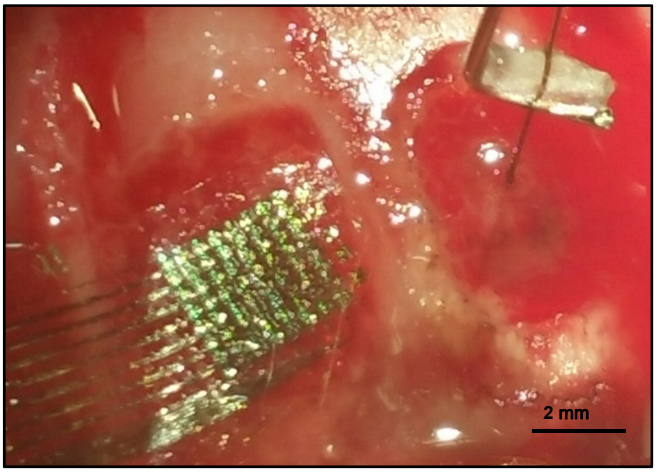

Supplementary Figure S21 | Photograph of an implanted 8x8 actively multiplexed array (left hemisphere of rat brain) and a control electrode (right hemisphere of rat brain).

© 2016 Macmillan Publishers Limited. All rights reserved.

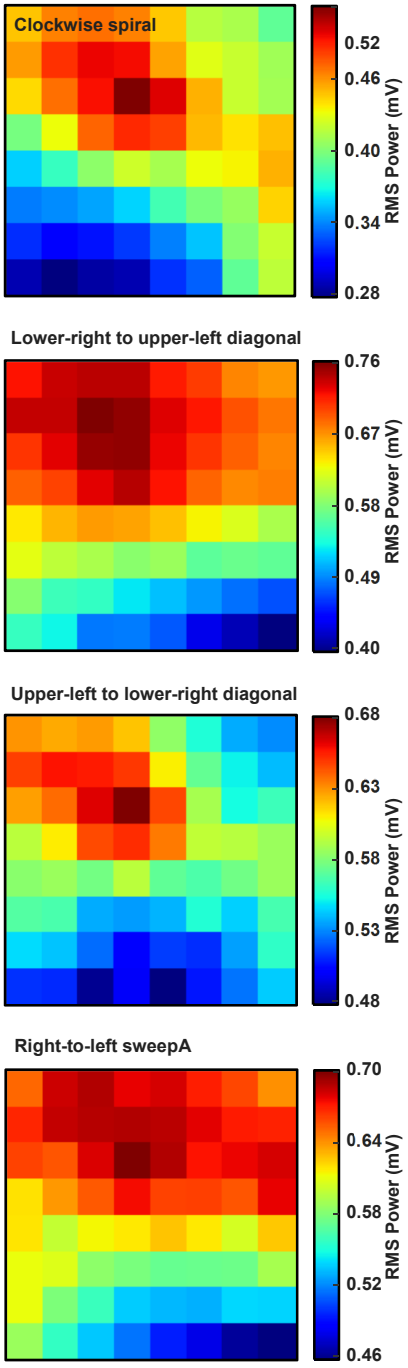

Supplementary Figure S22 | Representative RMS power image maps from four different spike clusters (clockwise spiral, lower-right to upper-left diagonal, upper-left to lower-right diagonal, right-to-left sweep) illustrate the high sensitivity of the electrode array and the spatially localized nature of spikes.

© 2016 Macmillan Publishers Limited. All rights reserved.

Nutrients	Mo	P	SiO_2
Recommended Daily Intakes	45 mcg	700 mg	5-10mg
Upper Limits	2000mcg	4g	N/A

Element	Si (Source: food)
Average Daily Intakes	20-50 mg

Compound	Ammonia (byproduct of Si_3N_4)
Amount of Daily Production	17 g
In the blood	0.7-2 mg/L

*The amount of Si_3N_4 in a device is 264 mcg. The amount of ammonia generated by dissolution of the Si_3N_4 is 128.2 mcg.
*Literature studies report a geographical correlation between the prevalence of Alzheimer's disease (AD) or various adverse effects on the central nervous system (CNS) in human brain and the concentration of aluminium ions (Al) in the brain from drinking water supplies[5,6]. The level of Al ions in the body can be significantly reduced by $SiOH_4$ (byproduct of dissolution of Si and SiO_2) by forming hydroxy-aluminosilicates (HAS)[6]. Studies also suggest that silicon-rich mineral waters can reduce the burden of aluminium in both Alzheimer's patients and control group[7].

Supplementary Table 1 | Recommended daily intake and upper limits[1] for injestion of Mo, P and SiO_2, average daily intake of Si from food[2,3], and amounts in the blood and daily production of ammonia for adults[4].

© 2016 Macmillan Publishers Limited. All rights reserved.

References

1. http://iom.nationalacademies.org/Activities/Nutrition/SummaryDRIs/DRI-Tables.aspx

2. Pennington, J. A. T. Silicon in foods and diets Food. *Addit. Contam.* **8**, 97-118 (1991).

3. Jugdaohsingh, R. *et al*. Dietary silicon intake and absorption. *Am. J. Clin. Nutr.* **75**, 887–893 (2002).

4. Syracus research coporations. Toxicological profile for ammonia. (2004).

5. Kawahara, M, & Kato-Negishi, M. Link between aluminum and the pathogenesis of Alzheimer's Disease: the integration of the aluminum and amyloid cascade hypotheses. *Int. J. Alzheimer's Dis.* **2011**,276393 (2011).

6. Jurkic, L. M., Cepanec, I., Pavelic, S. K., & Pavelic, K. Biological and therapeutic effects of ortho-silicic acid and some ortho-silicic acid-releasing compounds: new perspectives for therapy. *Nutr. Metab*. **10**, 2-12 (2013).

7. Davenward, S. *et al*. Silicon–rich mineral water as a non-invasive test of the 'aluminum hypothesis' in Alzheimer's disease. *J Alzheimers Dis*. **33**, 423–430 (2013).

© 2016 Macmillan Publishers Limited. All rights reserved.